THE GEOLOGICAL SOCIETY OF AMERICA®

Tectonic evolution of the Chinese Tianshan Orogen from subduction to arc-continent collision: Insight from polyphase deformation along the Gangou section, Central Asia

Pengfei Li[1,2,†], Min Sun[3], Gideon Rosenbaum[4], Keda Cai[5], Chao Yuan[1,2], Fred Jourdan[6], Xiaoping Xia[1,2], Yingde Jiang[1,2], and Yunying Zhang[3]

[1]*State Key Laboratory of Isotope Geochemistry, Guangzhou Institute of Geochemistry, Chinese Academy of Sciences, Guangzhou 510640, China*

[2]*Institutions of Earth Science, Chinese Academy of Sciences*

[3]*Department of Earth Sciences, The University of Hong Kong, Pokfulam Road, Hong Kong, China*

[4]*School of Earth and Environmental Sciences, The University of Queensland, Brisbane 4072, Queensland, Australia*

[5]*Xinjiang Research Center for Mineral Resources, Xinjiang Institute of Ecology and Geography, Chinese Academy of Sciences, Urumqi 830011, China*

[6]*Western Australian Argon Isotope Facility, Department of Applied Geology and JdL Centre, Curtin University, GPO Box U1987, Perth, Western Australia 6845, Australia*

ABSTRACT

The Central Asian Orogenic Belt, as the largest accretionary orogen on Earth, is an ideal candidate to study the geodynamics of convergent plate boundaries through a prolonged period. The evolution of this orogen has been explained by different tectonic models, which incorporated one, or a combination, of the following mechanisms: lateral stacking of arc systems along major shear zones, arc amalgamation, oroclinal bending, and trench migration. Here we elucidate major mechanisms responsible for the tectonic evolution of the Central Asian Orogenic Belt, focusing on the Chinese Tianshan Orogen in the southern Central Asian Orogenic Belt. Structural observations from the ~50-km-long Gangou section show evidence of polyphase deformation. The earliest episode of orogen-parallel sinistral shearing, constrained to the Early Devonian (ca. 399 Ma) by syn-deformational intrusions, was possibly controlled by oblique subduction. This was followed by an episode of ~NE–SW contractional deformation, dated at ca. 356 Ma ($^{40}Ar/^{39}Ar$ age of syn-deformational hornblende), and likely associated with an episode of trench advance. The third stages of deformation during the latest Carboniferous and Permian involved ~NE-SW contraction, orogen-parallel extension, and dextral transpression. Our new geochronological data constrain the timing of orogen-parallel extension to ca. 303–293 Ma, and confirm that dextral activation along shear zones occurred during the Permian. The results highlight the role of trench migration, oblique tectonics, and syn-collisional orogen-parallel extension in the build-up of the Central Asian Orogenic Belt, and contribute to the pre-collisional reconstruction of this orogenic system.

INTRODUCTION

Accretionary orogens are developed along convergent plate boundaries and are characterized by a long-lived history of subduction. Such orogens are major sites of continental growth and mineralization (Jahn, 2004; Cawood et al., 2009; Safonova et al., 2011; Cawood and Hawkesworth, 2015). The Central Asian Orogenic Belt, which is bounded by the Siberian Craton in the north and the Tarim and North China cratons in the south (Fig. 1), is a classic example of an accretionary orogen (Şengör et al., 1993; Şengör and Natal'in, 1996; Khain et al., 2002; Yakubchuk, 2004; Windley et al., 2007; Seltmann et al., 2014; Xiao et al., 2015, 2018). Its history of accretion is still controversial, however, with various models proposed for the evolution of the Central Asian Orogenic Belt. Processes incorporated in these models involve, for example, the lateral stacking of arc systems along a series of strike-slip shear zones (Şengör et al., 1993; Şengör and Natal'in, 1996; Şengör et al., 2018), the amalgamation of multiple arc systems (Windley et al., 2007; Xiao et al., 2015; Li et al., 2017), oroclinal bending (Van der Voo et al., 2006; Abrajevitch et al., 2008; Levashova et al., 2012; Yi et al., 2015), trench migration (e.g., Zhang et al., 2016; Han et al., 2016a; Wang et al., 2018), or combinations of the above processes (e.g., Li et al., 2018; Xiao et al., 2018; Li et al., 2019). In order to reconstruct the history of accretion in the Central Asian Orogenic Belt, it is important to understand the deformation history of each tectonic unit. This information can then be used to test various tectonic models, such as trench migration that commonly involves episodes of overriding plate contraction and extension.

The Tianshan Orogen in the southern Central Asian Orogenic Belt was formed by subduction processes at the southern branch of the Paleo-Asian Ocean and the subsequent collision between the Tarim Craton and island arcs. The orogen is made of a number of microcontinents, island and continental arcs, and accretionary complexes (Fig. 1; Charvet et al., 2007, 2011; Han et al., 2011; Xiao et al., 2013; Rojas-Agramonte et al., 2014; Degtyarev et al., 2017; Wang et al., 2018). Paleozoic accretion involved southward and/or northward subduction (current coordinates) of the Paleo-Asian oceanic plate below Precambrian microcontinents (Yili and Central Tianshan blocks, Fig. 1), and the development of the North Tianshan island arc system (e.g., Dananhu Arc, Fig. 1) (Allen et al., 1993a; Gao et al., 1998; Chen et al., 1999; Xiao et al., 2004; Charvet et al., 2007, 2011; Han et al., 2011; Xiao et al., 2013; Alexeiev et al., 2016; Wang et al., 2018). Following the closure of the Paleo-Asian

†pengfeili2013@gmail.com; pengfeili@gig.ac.cn.

GSA Bulletin; November/December 2020; v. 132; no. 11/12; p. 2529–2552; https://doi.org/10.1130/B35353.1; 15 figures; 1 table; Data Repository item 2020165. published online 8 April 2020

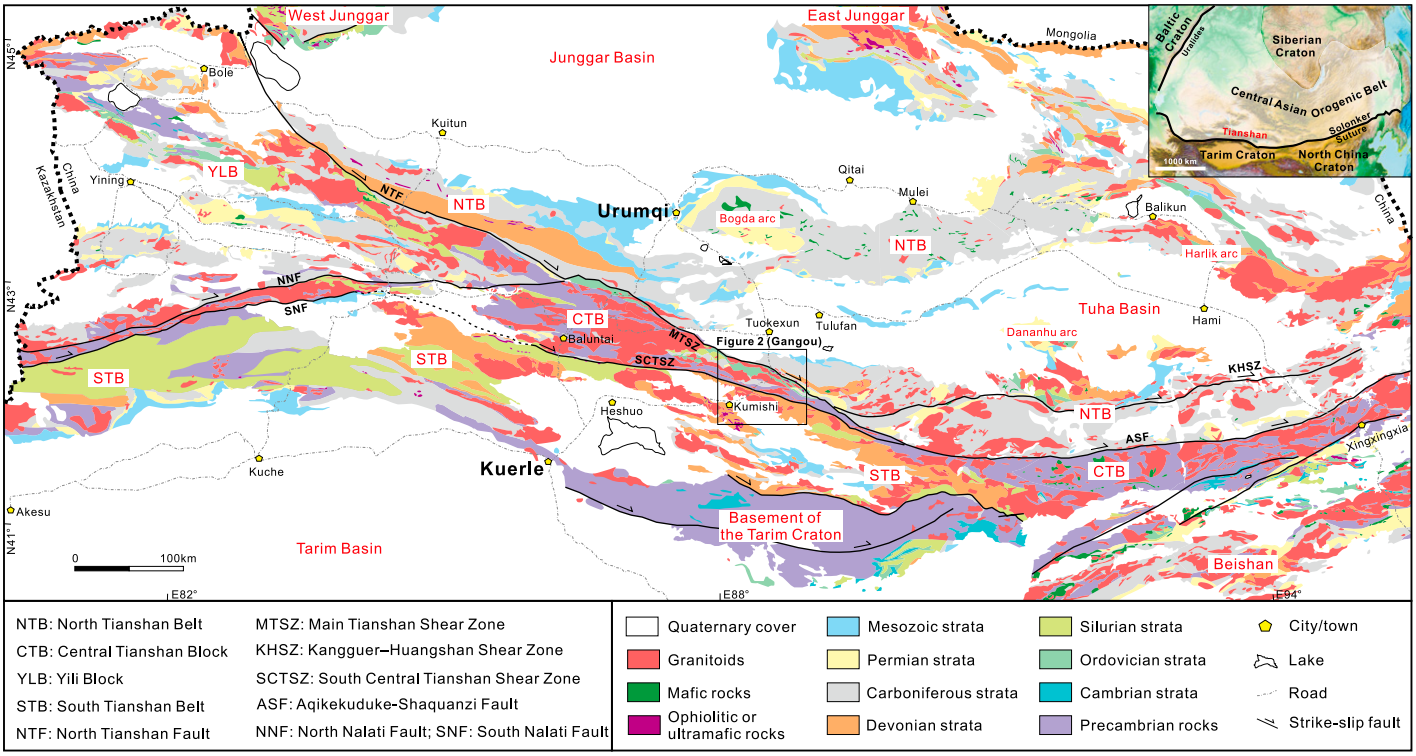

Figure 1. Geological map of the Chinese Tianshan Orogen (after Wang 2007). The inset topographic image is after Amante and Eakins (2009).

Ocean in the latest Paleozoic (e.g., Han et al., 2011; Xiao et al., 2013), the Tianshan Orogen evolved into a collisional phase, and the earlier accretion-related geological record was significantly overprinted. Previous studies have demonstrated that widespread dextral strike-slip shearing took place in the Tianshan Orogen during the Permian; together with evidence for folding, this deformation was attributed to the process of arc/continent amalgamation (Allen et al., 1995; Shu et al., 1999, 2002; Laurent-Charvet et al., 2003; Yang et al., 2007; de Jong et al., 2009; Lin et al., 2009; Wang et al., 2010a, 2011; Cai et al., 2012; Wang et al., 2014c). Pre-Permian strike-slip shear zones, folds and secondary foliations have also been documented (Gao et al., 1995; Laurent-Charvet et al., 2002; Deng et al., 2006; Lin et al., 2009; Wang et al., 2010a), but their tectonic significance has remained poorly understood.

This paper presents structural observations, new geochronological data, and tectonic synthesis of the middle segment of the Chinese Tianshan Orogen (Gangou section, Fig. 1) with the aim of reconstructing the deformational history and providing structural constraints on the evolution of the Chinese Tianshan Orogen. A particular effort was made to recognize polyphase structures, which together with zircon and monazite U-Pb dating and $^{40}Ar/^{39}Ar$ geochronology, allow us to better understand the structural evolution of the study area. The new results provide an insight into the role of oblique tectonics, trench migration, and arc amalgamation during the evolution of the Chinese Tianshan Orogen.

GEOLOGICAL SETTING

Chinese Tianshan Orogen

The Chinese Tianshan is an ~E-W orogenic belt that extends for ~1500 km and separates the Tarim Craton from the Junggar Basin and East/West Junggar terranes (Fig. 1). The mountainous topography was developed during the Cenozoic in response to far-field stresses associated with the collision of India and Asia (Avouac et al., 1993; Sobel and Dumitru, 1997; Tian et al., 2016). The geology of the Chinese Tianshan can be subdivided, from north to south, into the North Tianshan Belt, the Central Tianshan-Yili Block, and the South Tianshan Belt (Gao et al., 1998; Charvet et al., 2011; Xiao et al., 2013). Geographically, the Western Tianshan and the Eastern Tianshan are the two segments of the Chinese Tianshan to the west and east of the Urumqi-Kuerle meridian, respectively (Fig. 1).

The North Tianshan Belt in the Western Tianshan is made predominantly of late Paleozoic deep-marine turbidite interlayered with ophiolitic mélange, which were interpreted to represent part of an accretionary complex that developed adjacent to the Devonian–Carboniferous Yili arc farther south (Wang et al., 2006; Xiao et al., 2013). The North Tianshan Belt in the Eastern Tianshan consists of a series of Paleozoic island arcs (Bogda and Dananhu, Fig. 1), which are widely covered by Permian to Cenozoic sedimentary rocks of the Tuha Basin (Allen et al., 1993b; Wartes et al., 2002; Xiao et al., 2004).

The Central Tianshan–Yili Block is separated from the North Tianshan Belt by a strike-slip ductile shear zone (Main Tianshan Shear Zone; Fig. 1). The westward and eastward extensions of this shear zone are termed the North Tianshan Fault and the Aqikekuduke-Shaquanzi Fault, respectively. Previous work has shown a dominant dextral movement along this shear zone, and $^{40}Ar/^{39}Ar$ geochronological data constrained the timing of activity to ca. 290–244 Ma (Laurent-Charvet et al., 2003; Yang et al., 2007; Cai et al., 2012). To the south of this dextral shear zone, the triangle-shaped Yili Block, which only occurs in the Western Tianshan, is made of a Proterozoic basement, early Paleozoic carbonate, clastic rocks, intermediate to acid volcanic rocks, and a late Paleozoic volcano-sedimentary sequence (Yili Arc) (Gao et al., 1998; Zhou et al., 2001; Wang et al., 2007b; Xiao et al., 2013; Wang et al., 2014b; He et al., 2015; Huang et al., 2016;

An et al., 2017). Farther south, the Central Tianshan Block is separated from the Yili Block by a dextral strike-slip fault (North Nalati Fault; Fig. 1). The Central Tianshan Block comprises a Proterozoic basement (Huang et al., 2015, and references therein) overlain by Ordovician to Silurian volcano-sedimentary rocks and Carboniferous to Permian sedimentary rocks (BGMRX, 1993; Xiao et al., 2013). Within the Central Tianshan Block, the Central Tianshan Arc is defined by widespread Paleozoic calc-alkaline magmatic rocks (e.g., Charvet et al., 2007; Gao et al., 2009; Dong et al., 2011; Ma et al., 2014; Chen et al., 2015).

The South Tianshan Belt consists mainly of middle to late Paleozoic marine sedimentary rocks, subordinate ophiolites, and volcanic rocks, which are affected by a series of imbricated thrusts (Brookfield, 2000; Burtman, 2006; Gao et al., 2009; Biske and Seltmann, 2010; Han et al., 2011; Wang et al., 2011; Xiao et al., 2013; Jiang et al., 2014; Alexeiev et al., 2015). Recent radiometric dating from the ophiolitic rocks yielded ages in the range of 423–309 Ma (Han et al., 2015 and references therein; Wang et al., 2018). An (ultra)high-pressure metamorphic complex that experienced peak metamorphism at ca. 324–312 Ma exists along the northern margin of the South Tianshan Belt in the Western Tianshan (Fig. 1) (Klemd et al., 2011; Li et al., 2011; Yang et al., 2013; Zhang et al., 2013; Tan et al., 2019).

Geology of the Gangou Section

The Gangou section is exposed along the Urumqi–Kuerle road (Fig. 2). The following lithological description (Fig. 3) is based on the regional geological map (Kumishi sheet; BGMRX, 1959) and our field observations.

North Tianshan Belt

The oldest rocks in the North Tianshan Belt along the Gangou section belong to the Lower Carboniferous Xiaorequanzi Formation. These rocks are dominated by dark coarse-grained volcaniclastic rocks interlayered with andesite. They are conformably overlain by the Lower Carboniferous Yamansu Formation, which comprises andesite, volcaniclastic rocks, and minor clastic sedimentary rocks. The Upper Carboniferous Dikan'er Formation, which consists mainly of conglomerate, sandstone, and tuff, shows an angular unconformity with the underlying rocks (BGMRX, 1959). The Paleozoic rocks are overlain by the Sangonghe Formation (Jurassic sandstone) and Shanshan Group (Cenozoic reddish sandstone and conglomerate).

A zone of ophiolitic mélange occurs along the Main Tianshan Shear Zone, which marks the southern boundary of the North Tianshan Belt. Based on geochemical considerations, a supra-subduction origin has been inferred for this ophiolite (Dong et al., 2006). The mélange includes serpentinite, chert, and marble blocks within a matrix of meta-greywacke and mica schist (Dong et al., 2006; Wang et al., 2010b).

The Kangguer-Huangshan Shear Zone in the Eastern Chinese Tianshan merges westward with the Main Tianshan Shear Zone (Fig. 1) (Wang, 2007). The Carboniferous volcanic and sedimentary rocks of the North Tianshan Belt along the Gangou section may represent the westward extension of the Dananhu arc (Fig. 1).

Central Tianshan Block

Rocks from the Central Tianshan Block along the Gangou section belong to the Precambrian Xingxingxia Group, Ordovician to Silurian Ahabulake Group, Lower Carboniferous Ma'anqiao Formation, and the Permian Aqikebulake Formation (Fig. 3). The Xingxingxia Group is predominantly made of orthogneiss, paragneiss, quartzite, mica schist, amphibolite, and marble (Hu et al., 2000).

The Ahabulake Group is dominated by shallow-marine meta-sedimentary rocks and volcanic rocks, including dark green chlorite schist and mica schist (BGMRX, 1959). These rocks were deposited in the Ordovician–Silurian (Liu et al., 1988), possibly in a continental island arc (Charvet et al., 2007). The Ahabulake Group is unconformably overlain by the Ma'anqiao Formation, which consists mainly of Lower Carboniferous reddish conglomerate, and interlayered limestone, sandstone, and siltstone. The early Permian Aqikebulake Formation locally outcrops within the Central Tianshan Block, and is represented mainly by gray-green conglomerate and sandstone that show an angular unconformity with the underlying strata (BGMRX, 1959).

Granitoids are widespread in the Central Tianshan Block along the Gangou section. The earlier phase of granitic magmatism, in the Late Ordovician to Devonian, was characterized by S- and I-type granitoids that were likely associated with the subduction (Shi et al., 2007; Dong et al., 2011; Chen et al., 2015). The second phase of magmatism, in the Permian, is represented by A-type granitoids of a possible post-orogenic origin (Dong et al., 2011).

South Tianshan Belt

The South Tianshan Belt is separated from the Central Tianshan Block by the South Central Tianshan Shear Zone (also termed the Sangshuyuanzi Shear Zone or Baluntai Fault; Fig. 2). Rocks in the South Tianshan Belt include Early to Middle Devonian mica schist, quartz schist, and marble (Aerbishimaibulake and Alatage formations). A gray-green lithological layer of chlorite mica schist and marble defines a regional-scale antiform (Fig. 2) (BGMRX, 1959; Yang and Wang, 2006; Yang et al., 2007). Igneous rocks in the South Tianshan Belt are predominantly S-type granitoids of both Devonian (foliated) and Permian (non-foliated) ages (Yang and Wang, 2006; Chen et al., 2013; Chen et al., 2015).

STRUCTURAL GEOLOGY

We divided the study area into six structural domains (Fig. 2). Domains 1–3 (North Tianshan Belt) are separated from Domains 4 and 5 (Central Tianshan Block) by the Main Tianshan Shear Zone. Domain 6 is located in the South Tianshan Belt.

North Tianshan Belt

Rocks in the North Tianshan Belt are folded and faulted. In Domain 1, a south-dipping reverse fault separates north-dipping Jurassic rocks of the Sangonghe Formation from flat-lying Cenozoic rocks of the Shanshan Group (Figs. 4, 5A, and 5B). This fault zone was also responsible for locally thrusting Upper Carboniferous rocks of the Dikan'er Formation over the flat-lying Cenozoic Shanshan Group (Fig. 5C). The Cenozoic strata are folded adjacent to the fault zone (Fig. 5D). Farther south, the Upper Carboniferous Dikan'er Formation in Domain 2 is folded (subhorizontal NW-SE fold hinge and upright to inclined axial plane) and faulted (Figs. 4 and 5E), accommodating ~NE–SW contraction. The boundary between Domain 2 (Dikan'er Formation) and Domain 3 (Lower Carboniferous Yamansu Formation) is a southwest-dipping reverse fault (Figs. 4 and 5F). In Domain 3, a secondary foliation is recognized, defined by the alignment of lens-shaped clasts (Figs. 5G–5I). The foliation is commonly steeply dipping to SSW and is generally subparallel to bedding (Fig. 5J); however, an oblique foliation relative to bedding was also observed (Figs. 4 and 5K). The axial plane of mesoscopic folds is parallel to the secondary foliation (Fig. 5L), indicating that the fabric in Domain 3 is an axial plane foliation. The axial plane foliation becomes more penetrative toward the south, indicating a progressive increase in strain southward.

The Main Tianshan Shear Zone is characterized by the occurrence of an ~2-km-wide mylonitic zone (Figs. 2 and 4). The mylonitic fabric is steeply dipping to the NNE or SSW, and the stretching lineation is shallowly plunging to the ESE or WNW (Figs. 4 and 6A). S-C fabric, C′ shear band, sigmoidal mica fish, and asymmetric strain shadow around garnet porphyroblasts

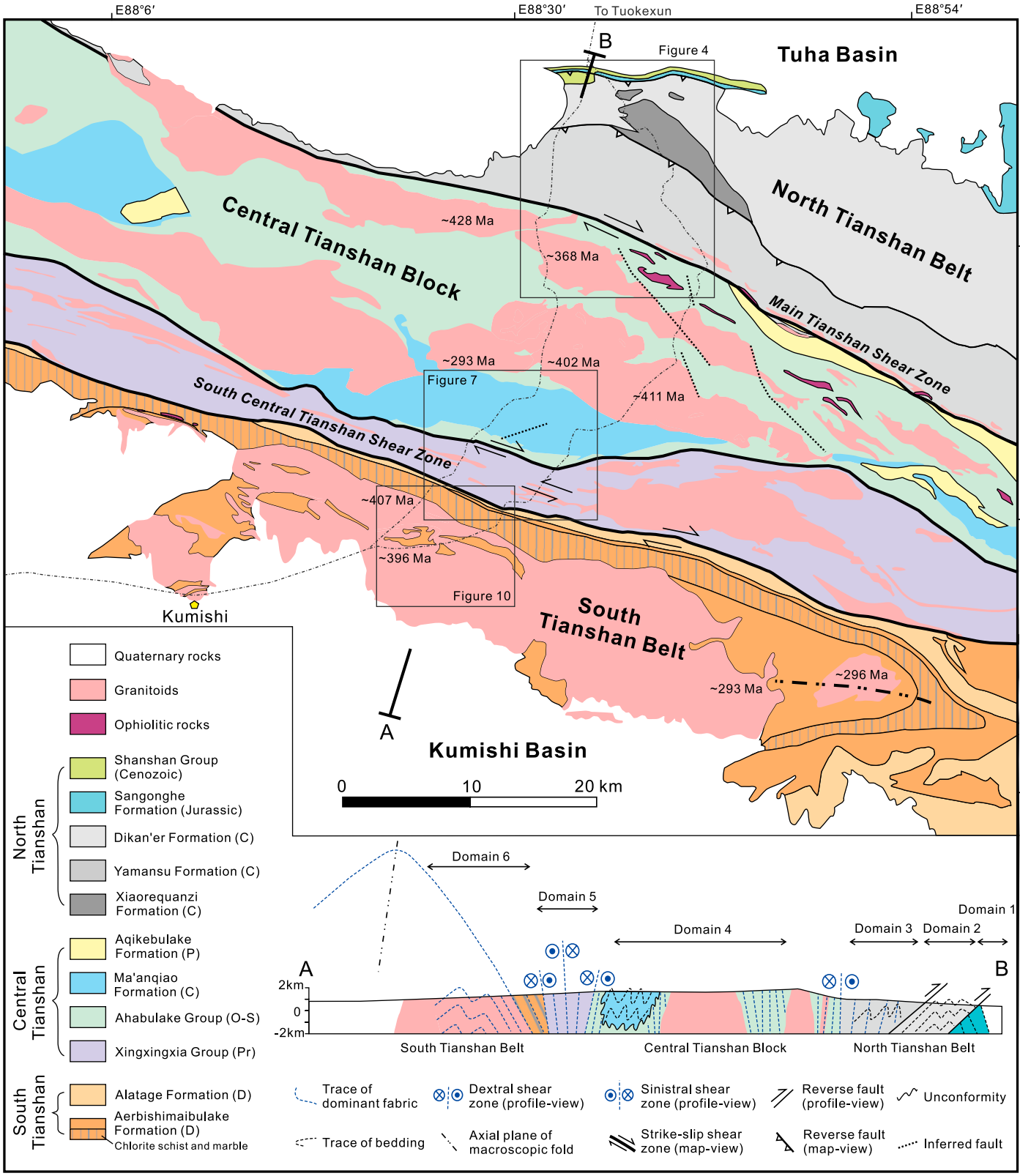

Figure 2. Geological map and cross section of the Gangou section (see location in Figure 1; BGMRX, 1959; Allen et al., 1993a). Zircon U-Pb ages of granitoids are from Chen et al. (2013, 2015), Shi et al. (2007), Dong et al. (2011), and Yang and Wang (2006). The macroscopic antiform in the South Tianshan Belt is defined by a gray-green lithological layer of chlorite-mica-schist and marble; the Permian granitoids in the core of the macroscopic antiform are non-foliated. Abbreviations: Permian (P), Carboniferous (C), Devonian (D), Ordovician to Silurian (O-S), Precambrian (Pr).

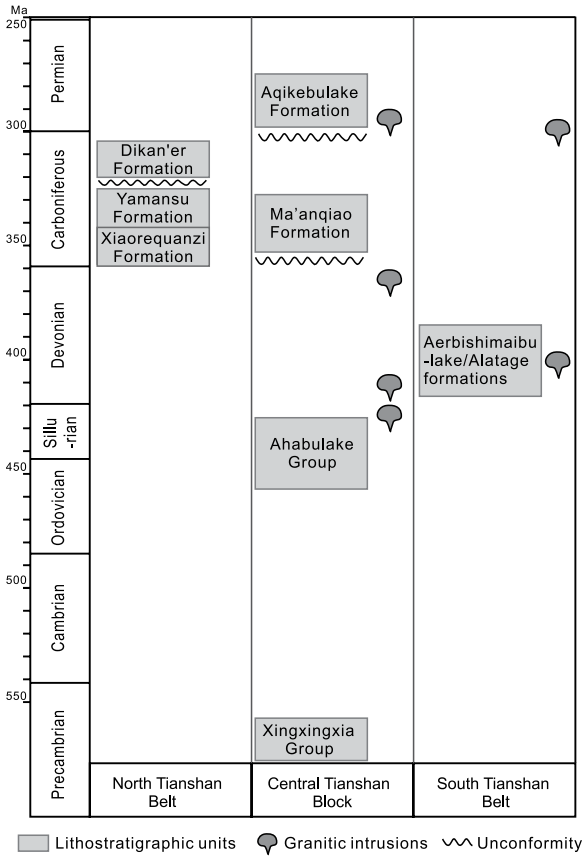

Figure 3. Simplified time-space diagram showing major lithostratigraphic units and granitic intrusions in the area of the Gangou section.

suggest a dextral movement along this shear zone (Figs. 6B–6F). The occurrence of sillimanite within the S-C fabric constrains the temperature during shearing to >500 ± 50 °C (Demange, 2012), consistently with evidence for high-temperature dynamic recrystallization of quartz by grain boundary migration (Fig. 6E). A NNE-directed thrust that crosscuts the mylonitic fabric indicates brittle reactivation of the Main Tianshan Shear Zone (Fig. 6G).

Central Tianshan Block

Structures in Domain 4

Domain 4 is dominated by Ordovician–Silurian and Carboniferous low-grade meta-sedimentary/volcanic rocks (Fig. 7A), with an angular unconformity between the two stratigraphic units (Fig. 3). A steeply dipping penetrative foliation (Figs. 8A and 8B), oriented ~NW–SE (Figs. 7A and 7C), is recognized in the Ordovician–Silurian rocks (Ahabulake Group). Outcrop-scale folds are also recognized and their axial planes are parallel to the penetrative foliation (Fig. 8C).

Carboniferous rocks (Ma'anqiao Formation) in Domain 4 are folded (Figs. 7A and 8D), with fold hinges moderately plunging to the SE (Figs. 7D and 7F). Exposures of the older (Ordovician–Silurian) rocks both in the northern and the southern sides of the Carboniferous rocks suggest the existence of a map-scale syncline. A steeply dipping ~NW–SE axial plane cleavage is recognized (Fig. 7E), showing variable angles relative to bedding (Figs. 8E and 8F). The axial plane cleavage is best developed in the core area of the map-scale syncline, and is undeveloped away from the core. In the lower part of the Ma'anqiao Formation, non-foliated limestone and siltstone unconformably overlie foliated rocks of the Ahabulake Group (Fig. 8G). Clasts of dark-green quartz schist with variable foliation orientations occur in the basal conglomerate of the Ma'anqiao Formation (Fig. 8H), and are likely sourced from the underlying Ahabulake Group (based on the similarity in lithology and structure). Overall, the structural observations indicate that the penetrative fabric in the Ahabulake Group was developed prior to the deposition of the Lower Carboniferous Ma'anqiao Formation.

Structures in Domain 5

Rocks in Domain 5 are predominantly high-grade metamorphic rocks of the Xingxingxia Group, but the exact metamorphic grade is not well constrained due to the lack of index minerals. Based on our field observations, we define three lithostratigraphic units within this group (Fig. 7A). In the south, Unit 1 consists mainly of mica schist, quartz schist, biotite plagioclase gneiss, quartzofeldspathic gneiss, quartzite, migmatite, and minor granitic gneiss and marble. Unit 2, in the central part (Fig. 7A), comprises reddish augen granitic gneisses interlayered with dark biotite-plagioclase gneiss, migmatite, and amphibole-biotite-plagioclase schist. Unit 3, in the north, comprises mica schist, biotite-plagioclase gneiss, quartzofeldspathic gneiss, migmatite, and minor augen K-feldspar gneiss. Rocks of all three units (Domain 5) show a widespread mylonitic fabric that defines the South Central Tianshan Shear Zone. The shear zone is characterized by a sinistral mylonitic shear zone bounded by two dextral mylonitic zones (Fig. 7A). Non-foliated granitoids occur along the sinistral mylonitic zone. These granitoids crosscut the mylonitic fabric, but show a map-view sigmoidal shape indicative of sinistral shearing (Figs. 8I and 8J).

Mylonitic fabric in the central part of Domain 5 is steeply dipping and associated with a subhorizontal stretching lineation (Figs. 7G, 7H, and 9A). Sinistral kinematics is inferred from S-C fabric and the occurrence of sigma-shaped feldspar and lithic fragments (Figs. 9B and 9C). Microstructural evidence for quartz dynamic recrystallization through grain boundary migration (Fig. 9D) suggests high temperature (>500 °C) shearing (Stipp et al., 2002). In a map view, slight variations in the orientations of the shear fabric may define regional-scale sinistral S-C structure (Fig. 7A). Sinistral shearing deformation is heterogeneous within the central part of Domain 5, with stretching lineation and shear sense criteria better developed in mica-rich lithologies.

In the northern and southern parts of Domain 5, the mylonitic fabric is also steeply dipping and associated with the subhorizontal stretching lineation (Figs. 7I–7L, 9E, and 9G). S-C fabric, as well as sigma-shaped feldspar, however, indicate dextral kinematics (Figs. 9F and 9H). Microstructures in the northern mylonite zone show evidence for both grain boundary migration and subgrain rotation recrystallization of quartz (Figs. 9I and 9J), indicating shearing at moderately high temperature (~500 °C) (Stipp et al., 2002).

South Tianshan Belt

Rocks in Domain 6 (South Tianshan Belt) are characterized by a pervasive mylonitic fabric and a subhorizontal ~WNW–ESE stretching lineation (Fig. 10). The latter is commonly defined by oriented hornblende in amphibolite and stretched feldspar aggregates in granitic mylonite (Figs. 11A and 11B). Asymmetric

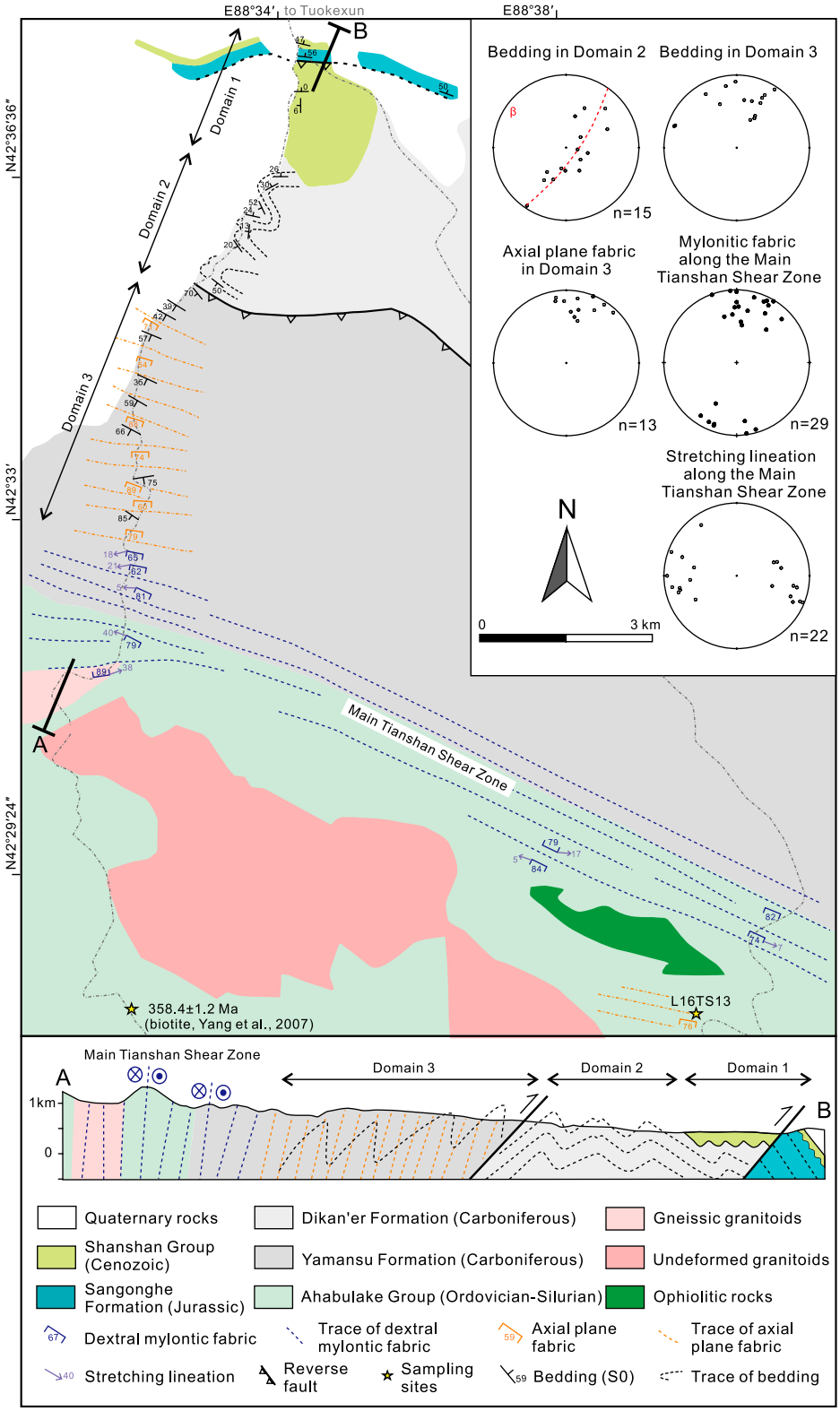

Figure 4. Structural map, cross section, and stereographic projections (lower hemisphere, equal area) of fabric elements in the North Tianshan Belt (for the location, see Fig. 2). All planar structures are plotted as poles. Note that the geometry of map-scale folds in Domain 3 is unconstrained due to strong bedding transposition.

quartz and feldspar porphyroclasts, as well as S-C fabric, indicate a top-to-ESE movement (Figs. 11C–11F). Evidence of polygonization (chessboard extinction of quartz; Fig. 11G) and grain boundary migration recrystallization (Fig. 11H) suggests high temperature (>500 °C) shearing (Stipp et al., 2002). In a macroscopic scale, the mylonitic fabric is folded with a steeply dipping axial plane trending ~E–W and a subhorizontal fold hinge oriented ~WNW–ESE (Figs. 10 and 11I). Macroscopic folds are also mimicked by the curved distribution of layered gabbro (Figs. 10 and 11J). This gabbro, which is non-foliated and occurs along the mylonitic fabric, was dated by U-Pb sensitive high-resolution ion microprobe (SHRIMP; zircon) and yielded an age of 302 ± 3 Ma (Xiao, 2013). The ~E–W macroscopic folds are not associated with an axial plane fabric, and are crosscut by undeformed mafic dikes (Fig. 10) composed of calc-alkaline lamprophyres (Allen et al., 1993a).

GEOCHRONOLOGY

U-Pb Geochronology

Sample Description

In order to constrain the timing of deformation, two granitic samples from the Central Tianshan Block were collected for zircon U-Pb analyses (Fig. 7A). Sample L17TS17 is from a non-foliated granitoid in Domain 5, which intruded into sinistral mylonitic zone (Fig. 8J). Sample L17TS87 is an augen granite from Unit 2 of the South Central Tianshan Shear Zone (Domain 5, Fig. 7A), which was affected by sinistral shearing.

Monazite U-Pb geochronology was conducted on three samples to constrain the timing of the top-to-ESE shear fabric (Fig. 10; for GPS coordinates see Table DR1[1]). Sample L17TS52 is a sheared (top-to-ESE) mica schist, comprising staurolite, sillimanite, muscovite, biotite, and garnet (Fig. 11E). Sample L17TS75 is an augen granitic gneiss, consisting of K-feldspar, plagioclase, quartz, and muscovite. Elongated K-feldspar aggregates define the stretching lineation associated with the top-to-ESE shear fabric (Fig. 11B). Sample L17TS43 is a sheared (top-to-ESE) granitic gneiss that contains mainly quartz, K-feldspar, plagioclase, muscovite, and biotite (Fig. 11C).

[1]GSA Data Repository item 2020165, Figure DR1, Tables DR1 and DR2, and Dataset DR1, is available at http://www.geosociety.org/datarepository/2020 or by request to editing@geosociety.org.

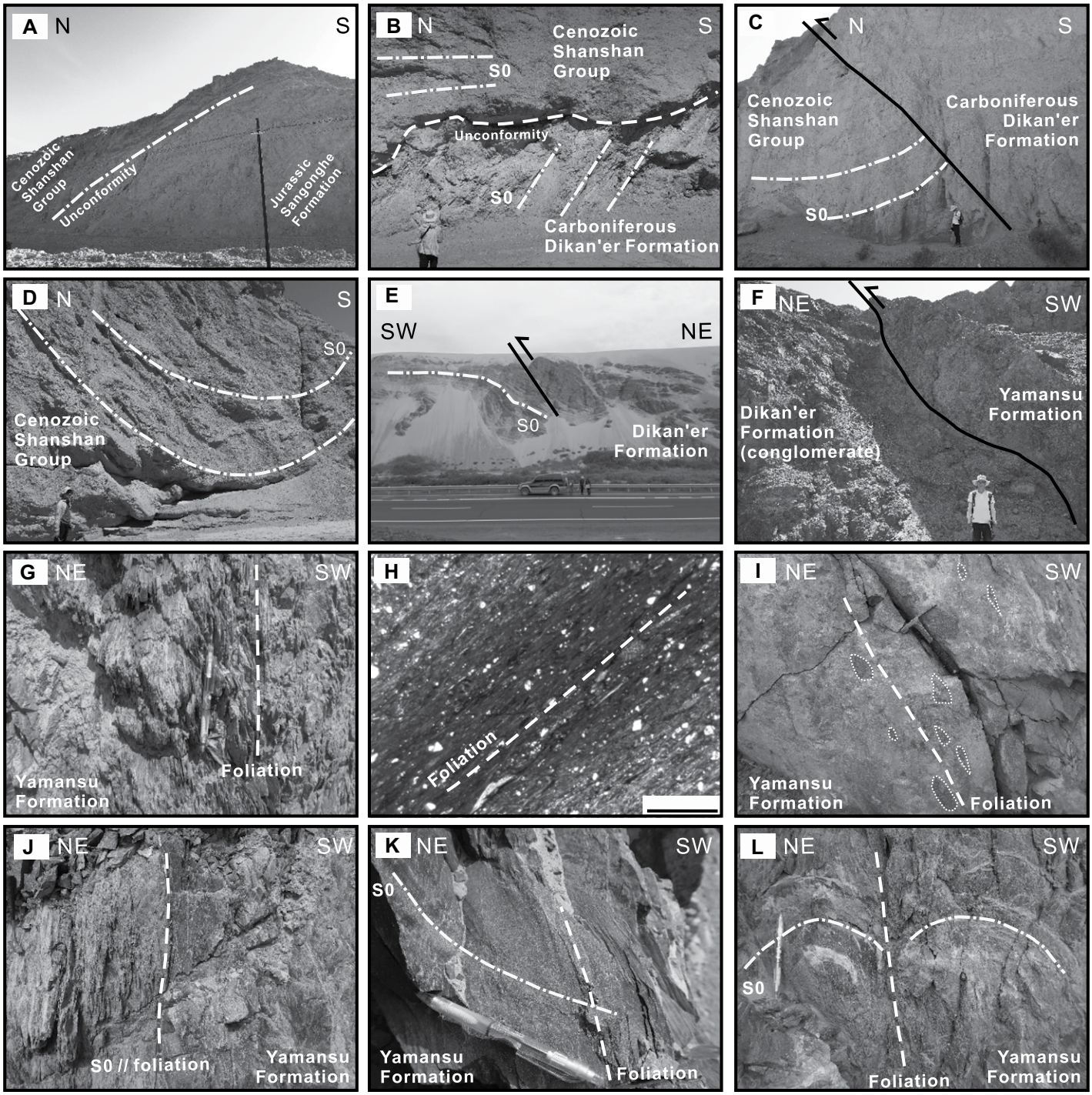

Figure 5. Photographs of structures in the North Tianshan Belt. (A) Cenozoic Shanshan Group unconformably overlying north-dipping strata of the Jurassic Sangonghe Formation. (B) Flat-lying Cenozoic rocks unconformably overlying Carboniferous rocks of the Dikan'er Formation. (C) South-dipping reverse fault separating the Carboniferous Dikan'er Formation from the Cenozoic Shanshan Group. (D) Folded Cenozoic rocks in the proximity of a reverse fault. (E) Folding associated with a north-dipping reverse fault (Dikan'er Formation). (F) Volcaniclastic rocks of the Yamansu Formation thrust northeastward over the Dikan'er Formation. (G–H) Slaty cleavage within the Yamansu Formation. (I) Preferred alignment of lens-shaped volcanic clasts defining a foliation (Yamansu Formation). (J) Parallelism between bedding (S_0) and foliation (Yamansu Formation). (K) Oblique intersection of bedding (S_0) with the foliation in the Yamansu Formation. (L) Foliation parallel to fold axial plane (Yamansu Formation). Note that the occurrence of an axial plane fabric (G–L) characterizes rocks in the Yamansu Formation in Domain 3 (Fig. 4). A color version of all photographs in this paper is attached in Figure DR1 (see text footnote 1).

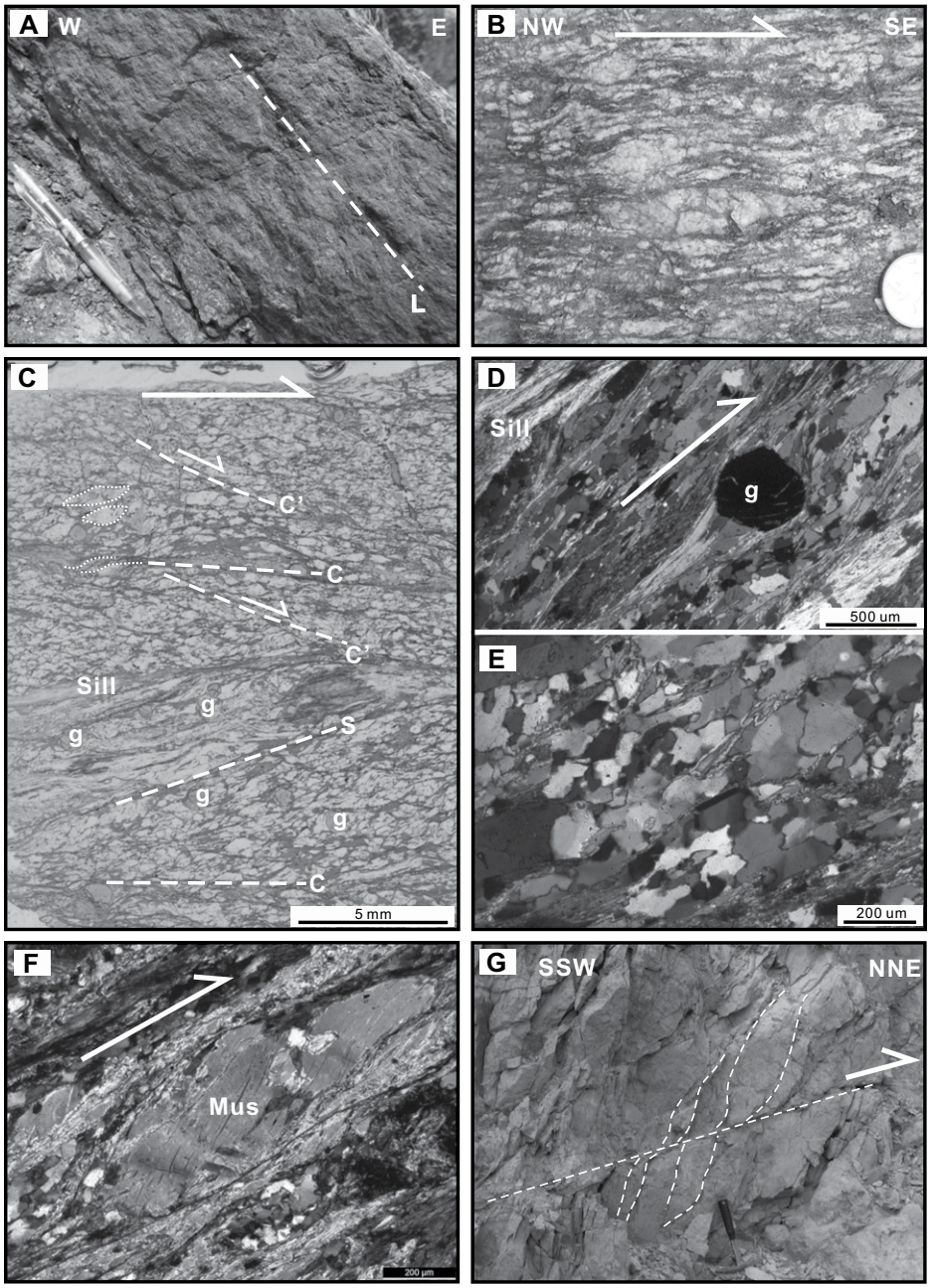

Figure 6. Photographs from the Main Tianshan Shear Zone. (A) Stretching lineation in mylonitic granitoid, defined by the alignment of quartz-feldspar aggregates. (B) Sigmoidal feldspar porphyroclasts illustrating dextral shear sense (horizontal view oriented subparallel to the stretching lineation). (C) S-C fabric, C′ shear bands, and sigmoidal porphyroclasts, indicating dextral shearing (plane-polarized light). Note the occurrence of sillimanite along the S-C fabric (sill: sillimanite; g: garnet). (D) Asymmetric strain shadow around garnet, showing dextral kinematics (cross-polarized light). (E) Irregular quartz grain boundaries indicating recrystallization by grain boundary migration (cross-polarized light). (F) Mica fish showing dextral shear sense (cross-polarized light; Mus: muscovite). (G) NNE-directed reverse fault within the Main Tianshan Shear Zone.

Methods

Zircon and monazite grains were mounted in epoxy resin and polished to expose a near equatorial section. Cathodoluminescence (CL) and backscattered electron (BSE) investigation was carried out to determine internal structures within grains.

Zircon U-Pb analyses were conducted using secondary ion mass spectrometry (SIMS) (CAMECA IMS1280-HR system) at the Guangzhou Institute of Geochemistry, Chinese Academy of Sciences. The analytical procedure is documented in Li et al. (2009). Calibration of Pb/U ratios was done relative to the Plešovice zircon standard (337.13 Ma) (Sláma et al., 2008), which was analyzed repeatedly after every four unknowns. The calibration was based on an observed linear relationship between $ln(^{206}Pb/^{238}U)$ and $ln(^{238}U^{16}O_2/^{238}U)$ (Whitehouse et al., 1997). A long-term uncertainty of 1.5% (1 relative standard deviation [RSD]) for $^{206}Pb/^{238}U$ measurements of standard zircon grains was propagated to the unknowns (Li et al., 2010), despite that the measured $^{206}Pb/^{238}U$ error in a specific session is generally around 1% (1 RSD) or less. U and Th concentrations of unknowns were also calibrated relative to the standard zircon Plešovice, with Th and U concentrations of 78 and 755 ppm, respectively (Sláma et al., 2008). Measured compositions were corrected for common Pb using non-radiogenic ^{204}Pb. The common Pb composition was assumed based on the model of Stacey and Kramers (1975). A secondary zircon standard, Qinghu (Li et al., 2013), was analyzed as unknown to monitor the reliability of the analysis. For the Qinghu zircon, 12 analytical spots were conducted, yielding a concordia age of 159.3 ± 1.4 Ma, which is identical (within error) to the recommended value of 159.5 ± 0.2 Ma (Li et al., 2013). Uncertainties on single analyses are reported at the 1σ level, whereas weighted mean ages for pooled U-Pb analyses are quoted with a 95% confidence interval. Data reduction was conducted with the software developed at NORDSIM by Dr. Martin Whitehouse. For the age calculation, we used the Isoplot 4.15 toolkit on Microsoft Excel (Ludwig, 2003).

Monazite U-Pb dating was conducted by laser ablation–inductively coupled plasma–mass spectrometry (LA-ICP-MS) at the Wuhan Sample Solution Analytical Technology Co., Ltd., Wuhan, China. Laser sampling was performed using a GeolasPro laser ablation system that consists of a COMPexPro 102 ArF excimer laser (wavelength of 193 nm and maximum energy of 200 mJ) and a MicroLas optical system. An Agilent 7700e ICP-MS instrument was used to acquire ion-signal intensities. Helium was applied as a carrier gas. Argon was used as the make-up gas mixed with the carrier gas via a T-connector before entering the ICP. A "wire" signal smoothing device is included in this laser ablation system, by which smooth signals are produced even at very low laser repetition rates down to 1 Hz (Hu et al., 2015). It is valid for in situ U-Pb dating of high-U minerals (Zong et al., 2015). The spot size and frequency of the laser were set to

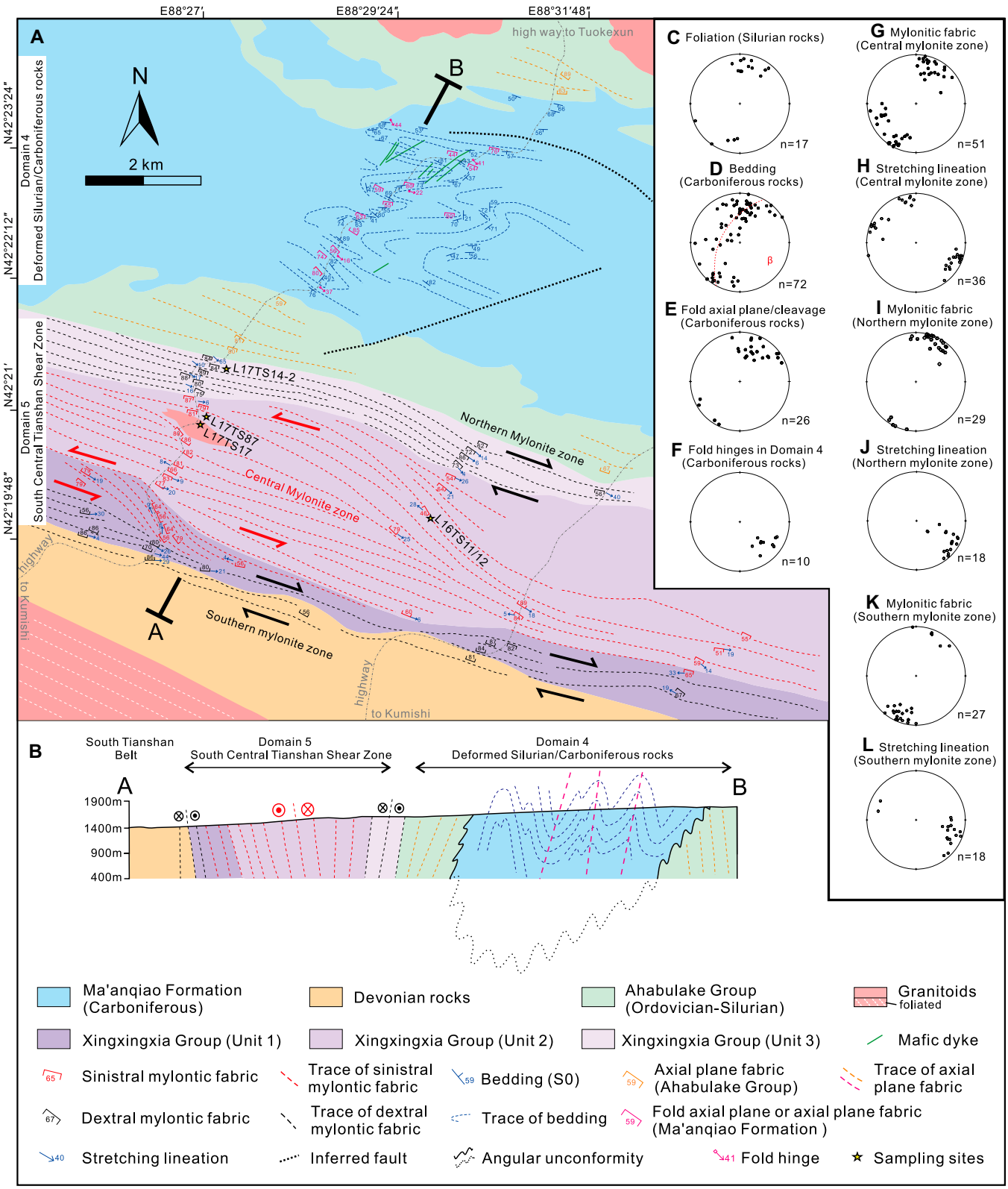

Figure 7. (A) Structural map of the Central Tianshan Block (see the location in Fig. 2). Note that the South Central Tianshan Shear Zone in Domain 5 includes dextral mylonitic zones in the north and south, and a sinistral mylonite zone in the center. Structural trends are based on the interpretation of satellite images (Dataset DR1; see footnote 1) and our observations. (B) Structural transect across the southern Central Tianshan Block. (C–L) Stereographic plots (lower hemisphere, equal area) for structural elements in Domains 4 and 5. All planar structures are plotted as poles.

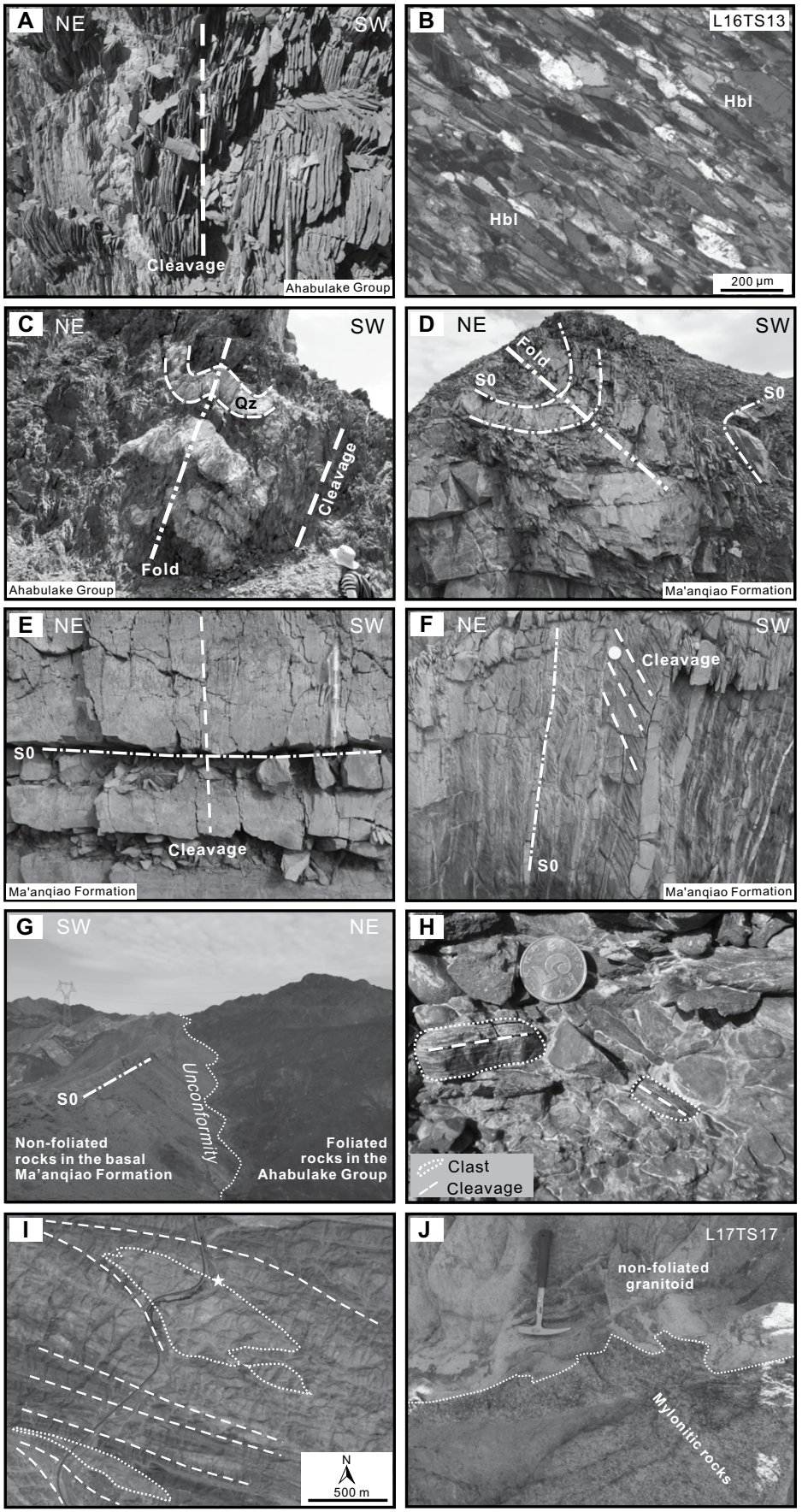

16 μm and 2 Hz, respectively. Monazite standard 44069 and glass NIST610 were taken as external standards for U-Pb dating and trace element calibration, respectively. Each analysis incorporated a background acquisition of ~20–30 s followed by 50 s of data acquisition from the sample. An Excel-based software ICPMSDataCal was used to perform offline selection and integration of background and analyzed signals, time-drift correction, and quantitative calibration for trace element analysis and U-Pb dating (Liu et al., 2008; Liu et al., 2010). Concordia diagrams and weighted mean calculations were done using the Isoplot 4.15 toolkit (Ludwig, 2003).

Results

CL images of selected analyzed zircon grains, and U-Pb analytical results, are presented in Figure 12 and Table DR1. Zircon grains from all samples are euhedral and show oscillatory zoning, thus indicating an igneous origin. After excluding the two youngest outliers, a weighted mean $^{206}Pb/^{238}U$ age of 399.1 ± 2.6 Ma (MSWD = 0.93) is obtained for other analyses of sample L17TS17. For sample L17TS87, a concordia age of 408.2 ± 3.0 Ma (MSWD = 0.31) was calculated.

Figure 8. Photographs of structures in the Central Tianshan Block (Domain 4). (A) Penetrative foliation in the Ordovician–Silurian Ahabulake Group. (B) Hornblende (Hbl) grains aligned along the foliation in an amphibole schist within the Ahabulake Group. (C) Folded quartz veins (Qz) with an axial plane parallel to the penetrative foliation (Ahabulake Group). (D) Folds in the Lower Carboniferous Ma'anqiao Formation. (E) Orthogonal relationships between bedding and cleavage (Ma'anqiao Formation). (F) Oblique relationships between bedding and cleavage (Ma'anqiao Formation). (G) Non-foliated limestone and minor siltstone layers in the lower Ma'anqiao Formation unconformably overlying foliated rocks of the Ahabulake Group (see A and B). (H) Clasts of foliated quartz schist in the basal conglomerate of the Ma'anqiao Formation, which are likely sourced from the underlying Ahabulake Group. Note variable foliation orientations in different clasts. (I) Satellite image showing the sigmoidal shape of non-foliated granitoids (dotted lines) within the sinistral central mylonite zone. The trace of the mylonitic fabric is shown by dash lines. The white star is the location of J. (J) Intrusive contact between a non-foliated granitoid and mylonite (oblique view).

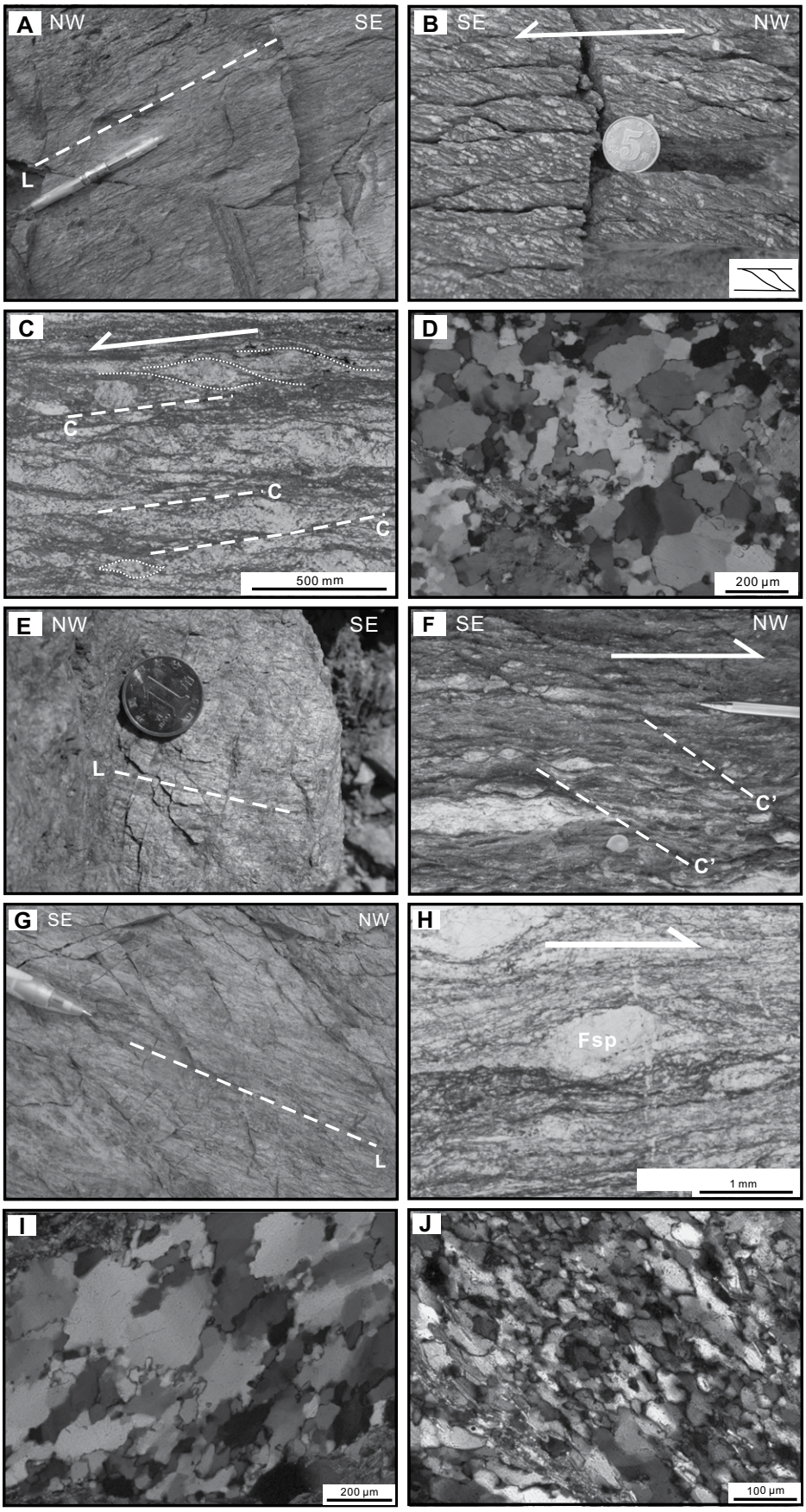

Monazite grains from three samples are 100–250 μm in size. Backscattered electron images show homogeneous or faint irregular zoning. In samples L17TS43 and L17TS52, most monazite ages are clustered tightly on the concordia curve (Fig. 12 and Table DR1). The few outliers with younger and discordant/subdiscordant ages may have resulted from variable disturbances of the U-Pb system. After excluding two outliers, a weighted mean $^{206}Pb/^{238}U$ age of 299.7 ± 2.3 Ma (MSWD = 2) was calculated for sample L17TS43 (Fig. 12C). A similar age of 299.1 ± 1.5 Ma (MSWD = 1.8) was obtained from sample L17TS52 after excluding three outliers (Fig. 12D). A weighted mean $^{206}Pb/^{238}U$ age of 303.7 ± 1.4 Ma (MSWD = 1.6) was calculated for sample L17TS75 (Fig. 12E).

$^{40}Ar/^{39}Ar$ Geochronology

Sample Description

Nine samples were analyzed by $^{40}Ar/^{39}Ar$ geochronology to constrain the timing of deformation along the Gangou section (Figs. 4, 7A, and 10, and Table 1). An amphibole schist sample (L16TS13) from the Ahabulake Group in the Central Tianshan Block (Domain 4, Fig. 4) comprises hornblende, quartz, and plagioclase, with

Figure 9. Photographs and photomicrographs of the South Central Tianshan Shear Zone in the Central Tianshan Block (Domain 5). (A) Stretching lineation in the central mylonite zone. (B–C) S-C fabric and sigmoidal quartz-feldspar aggregates demonstrating sinistral kinematics along the central mylonite zone (plane-polarized light for C). (D) Irregular quartz grain boundaries indicating grain boundary migration recrystallization within the central mylonite zone (cross-polarized light). (E) Stretching lineation in mica schist (northern mylonite zone). (F) C′ shearing bands showing dextral kinematics (northern mylonite zone). (G) Stretching lineation in mica schist (southern mylonite zone). (H) Dextral movement along the southern mylonite zone, defined by sigmoidal feldspar (Fsp) porphyroclasts (plane-polarized light). (I) Irregular quartz grain boundaries associated with grain boundary migration recrystallization (cross-polarized light). (J) Dynamically recrystallized quartz formed by subgrain rotation (cross-polarized light). All thin sections are cut parallel to stretching lineation and perpendicular to foliation. Horizontal view oriented subparallel to the stretching lineation for field photos (B and F).

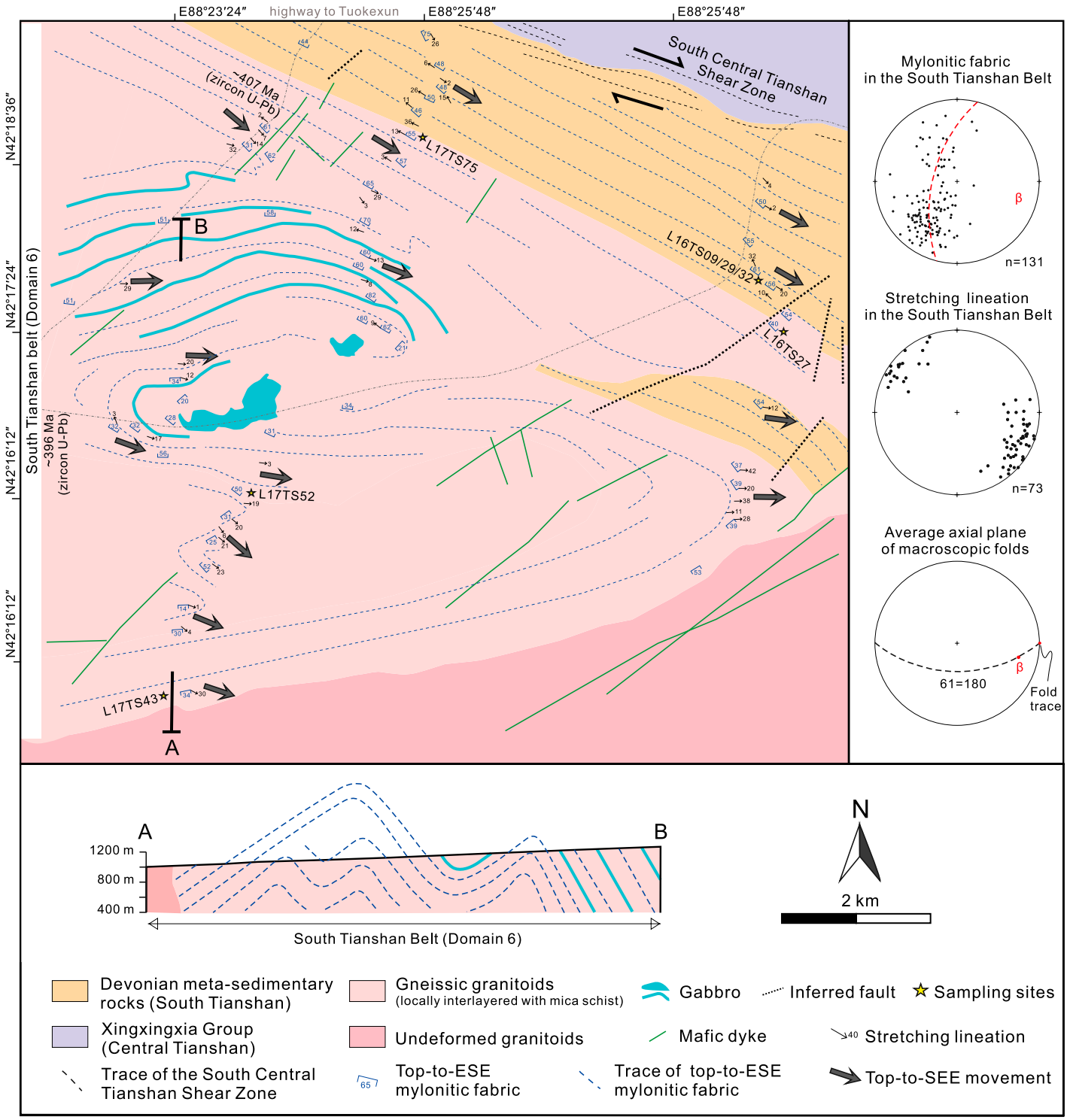

Figure 10. Structural map and transect of the South Tianshan Belt (for the location, see Fig. 2). Note that top-to-ESE shear fabric is folded to form ~E-W macroscopic folds with steeply dipping axial planes and fold hinges plunging to ~ESE. Structural trends are based on the interpretation of satellite images (Dataset DR1; see footnote 1) and our observations. Zircon U-Pb ages of granitoids are from Chen et al. (2015) and Yang and Wang (2006).

hornblende aligned along the foliation (Fig. 8B). One mica schist sample (L17TS14-2) with dextral shear fabric was collected from Unit 3 of the Xingxingxia Group (Central Tianshan Block, Domain 5; Fig. 7). Two mica schist samples (L16TS11 and L16TS12) with a pervasive sinistral shear fabric were taken from Unit 2 of the Xingxingxia Group (Central Tianshan Block, Domain 5; Fig. 7). Four samples were selected from the South Tianshan Belt (Domain 6; Fig. 10), where the mylonitic fabric shows top-to-ESE kinematics. Sample L16TS09 is an

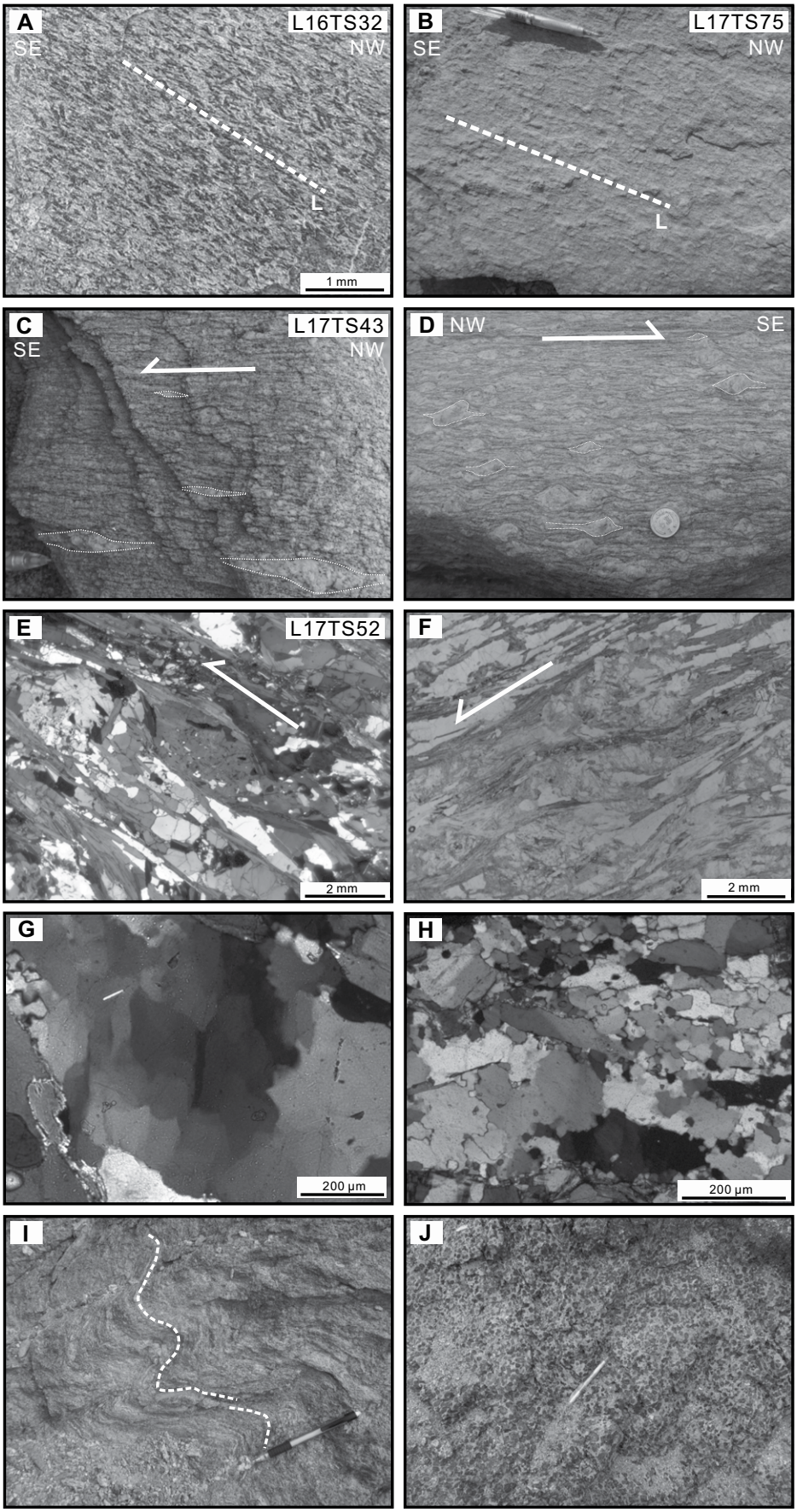

amphibole biotite schist, and sample L16TS29 is a staurolite mica schist. Sample L16TS27 is a mylonitic granitoid composed of quartz, K-feldspar, plagioclase, muscovite, and minor biotite. Sample L16TS32 was collected from an amphibolite layer, in which oriented hornblende grains define an ~NW–SE stretching lineation (Fig. 11A).

Methods

Samples were crushed and washed in distilled water and ethanol in an ultrasonic bath. We selected biotite from samples L16TS11 and L16TS09, muscovite from samples L16TS12, L17TS14-2, and L16TS27, and hornblende from samples L16TS32 and L16TS13. Both biotite and muscovite were selected from sample L16TS29. All crystals were carefully hand-picked under a binocular microscope. Samples were loaded into several large wells of one 1.9-cm-diameter and 0.3-cm-deep aluminum disc. These wells were bracketed by small wells that included Fish Canyon sanidine (FCs) used as a neutron fluence monitor for which an age of 28.294 ± 0.036 Ma (1σ) was adopted (Renne et al., 2011). The discs were Cd-shielded (to minimize undesirable nuclear interference reactions) and irradiated in the Oregon State University nuclear reactor (USA), in a central position, for 25 h. The mean J-value computed from standard grains within the small pits is 0.0108468 ± 0.0000174 (0.16%); it was calculated from the average and standard deviation of J-values of the small wells

Figure 11. Photographs and photomicrographs of structures in the South Tianshan Belt (Domain 6). (A) Amphibolite sample (L16TS32) with preferred alignment of hornblende that defines stretching lineation. (B) Stretching lineation defined by elongated K-feldspar aggregates in augen gneiss (sample L17TS75). (C–F) Top-to-ESE sense of shear in mylonitic fabric, indicated by asymmetric quartz, feldspar or quartz-feldspar aggregates. (G) Chessboard extinction in quartz. (H) Irregular quartz grain boundaries indicating grain boundary migration recrystallization. (I) Folded top-to-ESE mylonitic fabric. (J) Non-foliated gabbro intruded along the top-to-ESE mylonitic fabric. All thin sections are cut parallel to stretching lineation and perpendicular to foliation (plane-polarized light for F and cross-polarized light for E, G, and H). Horizontal view in C and D is oriented sub-perpendicular to the foliation and subparallel to the stretching lineation.

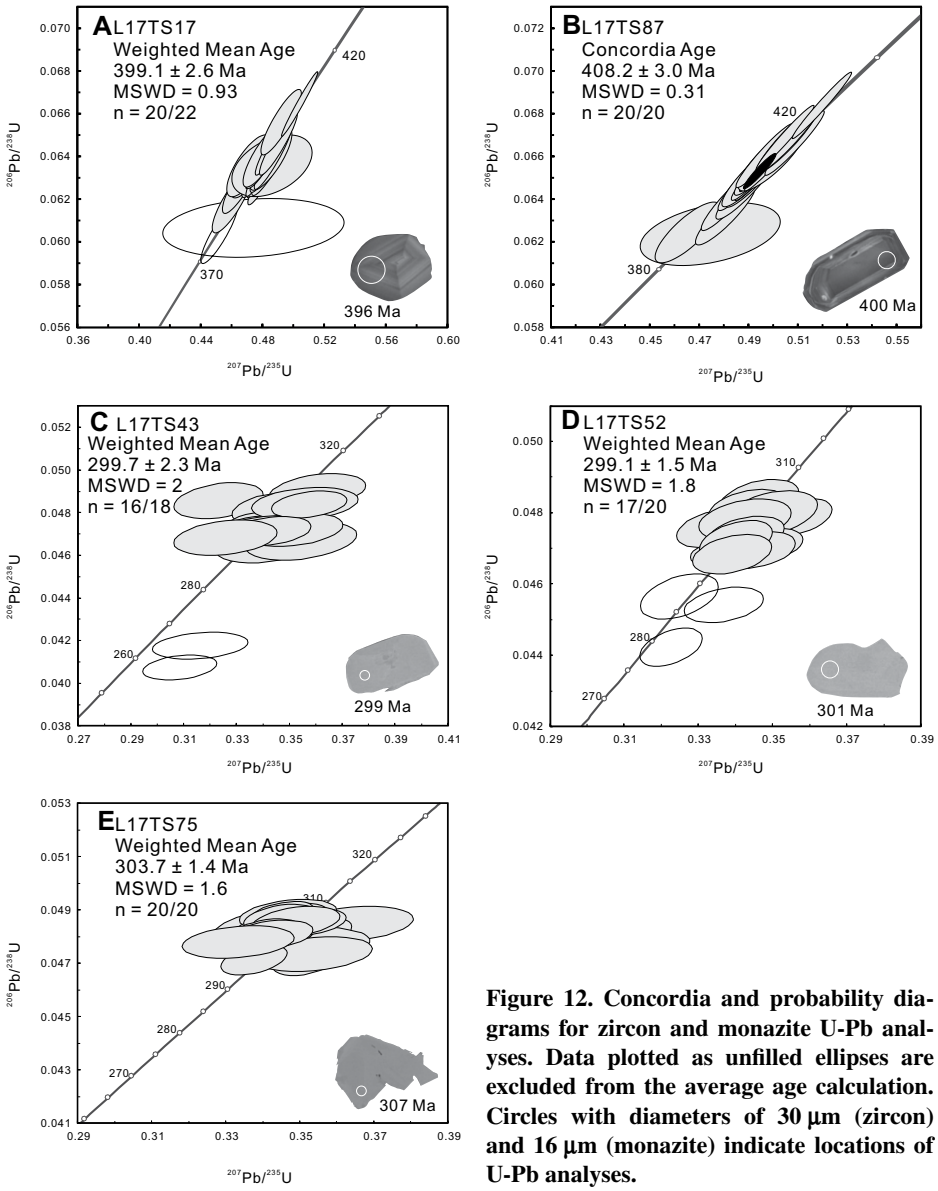

Figure 12. Concordia and probability diagrams for zircon and monazite U-Pb analyses. Data plotted as unfilled ellipses are excluded from the average age calculation. Circles with diameters of 30 µm (zircon) and 16 µm (monazite) indicate locations of U-Pb analyses.

for each irradiation disc. Mass discrimination was monitored using an automated air pipette, with values ranging from 0.99204 ± 0.00020 to 1.00415 ± 0.00030 per dalton (atomic mass unit) relative to an air ratio of 298.56 ± 0.31 (Lee et al., 2006). The correction factors for interfering isotopes were ($^{39}Ar/^{37}Ar$) Ca = 6.95×10^{-4} (±1.3%), ($^{36}Ar/^{37}Ar$) Ca = 2.65×10^{-4} (±0.84%) and ($^{40}Ar/^{39}Ar$) K = 7.30×10^{-4} (±12.4%) (Renne et al., 2013).

$^{40}Ar/^{39}Ar$ analyses were performed at the Western Australian Argon Isotope Facility (Curtin University). The samples were step-heated using a 110 W Spectron Laser Systems, with a continuous Nd-YAG (neodymium-doped yttrium aluminum garnet; infrared; 1064 nm) laser rastered over the sample during one minute to ensure a homogenously distributed temperature. The gas was purified in a stainless-steel extraction line using two SAES AP10 getters and a GP50 getter. Ar isotopes were measured in a static mode using a MAP 215-50 mass spectrometer (resolution of ~450; sensitivity of 4×10^{-14} mol/V) with a Balzers SEV 217 electron multiplier using 9–10 cycles of peak-hopping. The data acquisition was performed with the Argus program written by M.O. McWilliams and ran under a LabView environment. The raw data were processed using the ArArCALC software (Koppers, 2002) and the ages were calculated using the decay constants recommended by Renne et al. (2010). Blanks were monitored every three to four steps, and typical ^{40}Ar blanks range from 1×10^{-16} to 2×10^{-16} mol. Ar isotopic data corrected for blank, mass discrimination and radioactive decay are given in Table DR2 (see footnote 1), with individual errors given at the 1σ level.

Plateau ages were determined based on the following criteria: (1) a plateau must include at least 70% of ^{39}Ar; and (2) the plateau should be distributed over a minimum of three consecutive steps, agreeing at 95% confidence level, and satisfying a probability of fit (P) of at least 0.05. Plateau ages are given at the 2σ level and are calculated using the mean of all the plateau steps, each weighted by the inverse variance of their individual analytical error. Mini-plateaus are defined similarly except that they include between 50% and 70% of ^{39}Ar, thus providing a less reliable age. All sources of uncertainties are included in the calculation.

Results

Analytical results and age spectra are presented in Table 1, Table DR2, and Figure 13. Biotite grains from samples L16TS09 and L16TS29-2 in the South Tianshan Belt yielded two plateau ages of 295.5 ± 2.3 Ma and 293.3 ± 1.5 Ma, which are similar to two muscovite ages of 295.6 ± 1.3 (L16TS27) and 293.3 ± 1.6 Ma (L16TS29-1; Figs. 13A–13D). An additional hornblende sample (L16TS32) from the South Tianshan Belt yielded a plateau age of 298.6 ± 1.0 Ma (Fig. 13E) including ~75% of the total ^{39}Ar released, although we note that the plateau is distributed over only two large steps.

In the Central Tianshan Block, hornblende from the Ahabulake Group (sample L16TS13) in the Central Tianshan Block yielded a plateau age of 356.4 ± 6.5 Ma (Fig. 13F). Sample L16TS11 from the sinistral mylonitic zone of the South Central Tianshan Shear Zone yielded a plateau age of 247.7 ± 1.4 Ma (biotite; Fig. 13G). A muscovite sample (L16TS12) yielded a mini-plateau age of 249.4 ± 1.0 Ma with all but one of second to ninth steps, being concordant (P = 0.44) and including 66% of the total ^{39}Ar released (Fig. 13H). This age is treated with caution; we note that it is statistically indistinguishable from the biotite $^{40}Ar/^{39}Ar$ age albeit not robust enough to derive any cooling rate. Sample L17TS14-2 from the dextral mylonitic zone of the South Central Tianshan Shear Zone yielded a muscovite plateau age of 259.4 ± 0.9 Ma (Fig. 13I).

DISCUSSION

Timing of Deformation along the Gangou Section

North Tianshan Belt

Deformation in the North Tianshan Belt (Domain 1, Fig. 4) involved thrusting and folding of the Cenozoic Shanshan Group (Figs. 5C and 5D). This contractional deformation may

TABLE 1. SUMMARY OF NEW $^{40}Ar/^{39}Ar$ AGES

Sample no. (WGS84)	Latitude (°N)	Longitude (°E)	Tectonic unit	Deformation features	Dated minerals	Plateau ages (Ma)
L16TS09	42°17′54″	88°28′52″	South Tianshan Belt (Domain 6)	D_{S1} top-to-ESE shearing	Biotite	295.5 ± 2.3
L16TS27	42°17′25″	88°29′6″	South Tianshan Belt (Domain 6)	D_{S1} top-to-ESE shearing	Muscovite	295.6 ± 1.3
L16TS29-1	42°17′42″	88°29′9″	South Tianshan Belt (Domain 6)	D_{S1} top-to-ESE shearing	Muscovite	293.3 ± 1.6
L16TS29-2	42°17′42″	88°29′9″	South Tianshan Belt (Domain 6)	D_{S1} top-to-ESE shearing	Biotite	293.3 ± 1.5
L16TS32	42°17′51″	88°29′1″	South Tianshan Belt (Domain 6)	D_{S1} top-to-ESE shearing	Hornblende	298.6 ± 1.0
L16TS13	42°27′50″	88°40′12″	Central Tianshan Block (Domain 4)	D_{C2} axial planar fabric	Hornblende	356.4 ± 6.5
L16TS11	42°20′3″	88°29′46″	Central Tianshan Block (Domain 5)	D_{C1} sinistral shearing	Biotite	247.7 ± 1.4
L16TS12	42°20′3″	88°29′46″	Central Tianshan Block (Domain 5)	D_{C1} sinistral shearing	Muscovite	249.4 ± 1.0
L17TS14-2	42°21′24″	88°26′54″	Central Tianshan Block (Domain 5)	D_{C4} dextral shearing	Muscovite	259.4 ± 0.9

correspond to Cenozoic brittle reactivation along the Main Tianshan Shear Zone, which involved north-directed thrusting (Fig. 6G). Farther south, in Domains 2 and 3, ~NW–SE-trending folds and reverse faults affected Upper Carboniferous rocks of the Dikan'er Formation. This deformation, therefore, must have occurred during or after the latest Carboniferous.

Central Tianshan Block

Dextral shearing deformation along the Main Tianshan Shear Zone has been dated by $^{40}Ar/^{39}Ar$ geochronology. Laurent-Charvet et al. (2003) reported 269.1 ± 5.4 Ma muscovite $^{40}Ar/^{39}Ar$ plateau age and 244.7 ± 2.6 Ma biotite $^{40}Ar/^{39}Ar$ isochron age. Yang et al. (2009) dated syn-kinematic muscovite and biotite, which both yielded an $^{40}Ar/^{39}Ar$ plateau age of ca. 266 Ma, younger than a biotite $^{40}Ar/^{39}Ar$ plateau age of 290 ± 2.4 Ma reported by Cai et al. (2012). These $^{40}Ar/^{39}Ar$ ages may represent the timing of deformation or the cooling age of dated minerals through their closure temperature. Our microstructural observations show the occurrence of quartz recrystallization by grain boundary migration (Fig. 6E), which, together with evidence for prism <c> slip for quartz c-axis fabric (Cai et al., 2012), indicate high-temperature (up to ~650 °C) shearing. The appearance of middle to low temperature basal <a> and rhomb <a> slip for quartz c-axis fabric along the Main Tianshan Shear Zone (Laurent-Charvet et al., 2003; Cai et al., 2012) indicates multiple stages of shear deformation. Therefore, we suggest that the variable $^{40}Ar/^{39}Ar$ ages (ca. 290 Ma, 269–266 Ma, and ca. 244 Ma) from the syn-kinematic biotite and muscovite correspond to multiple stages of activity along the Main Tianshan Shear Zone. Farther south, dextral shearing along the South Central Tianshan Shear Zone (Domain 5 in Fig. 7) may have taken place at the same period, as indicated by the syn-deformational muscovite $^{40}Ar/^{39}Ar$ age (ca. 260 Ma) presented in this study (Fig. 13I).

Our structural observations recognized an episode of sinistral shearing along the South Central Tianshan Shear Zone (Domain 5). Similar kinematics has also been reported by Allen et al. (1993a), Laurent-Charvet et al. (2003), Yang et al. (2004), and Deng et al. (2006). The mylonitic granitoids affected by this deformation yielded a SIMS zircon U-Pb age of 408.2 ± 2.6 Ma (sample L17TS87 in this study; Fig. 12B), which provides a maximum constraint for the timing of sinistral shearing. The non-foliated granitoid (sample L17TS17), which intrudes the sinistral mylonitic zone (Fig. 8J), yielded a SIMS zircon U-Pb age of 399.1 ± 2.6 Ma (Fig. 12A). The dated non-foliated granitoid shows a macroscopic sigmoidal shape (Fig. 8I), which seems to indicate sinistral shearing, thus suggesting a (late) syn-kinematic emplacement. The ca. 399 Ma zircon age may thus represent the time of sinistral shearing along the South Central Tianshan Shear Zone. This age constraint is in agreement with a previously published muscovite $^{40}Ar/^{39}Ar$ age of 393 ± 6 Ma, which was obtained from sinistral mylonitic rocks associated with the South Central Tianshan Shear Zone (Deng et al., 2006). However, biotite and muscovite extracted from the sinistral mylonitic zone in this study yielded an $^{40}Ar/^{39}Ar$ plateau age of 247.7 ± 1.4 Ma and a near mini-plateau (MP) age of 249.4 ± 1.0 Ma (Figs. 7, 13G, and 13H), respectively. These new ages are considerably younger than the inferred ca. 399 Ma deformation age. Given that these ages coincide with the timing of dextral deformation, we assume that some of the syn-kinematic minerals within the sinistral mylonitic zone were thermally reset during the subsequent phase of dextral shearing.

Hornblende extracted from the cleavage domain within Ordovician–Silurian rocks of the Ahabulake Group (Domain 4) yielded an $^{40}Ar/^{39}Ar$ age of 356.4 ± 6.5 Ma (Fig. 13F), similarly to a previously reported $^{40}Ar/^{39}Ar$ biotite age (358.4 ± 1.2 Ma) from the Ahabulake Group (Fig. 4) (Yang et al., 2007). These $^{40}Ar/^{39}Ar$ ages may either represent the timing of fabric formation, or the age of cooling through the closure temperatures of the dated minerals. Given the relatively high closure temperature of hornblende (500–550 °C) and the lack of high-temperature metamorphic mineral assemblages (e.g., garnet or sillimanite) in the meta-sedimentary/volcanic rocks of the Ahabulake Group, we think that the interpretation of the $^{40}Ar/^{39}Ar$ age (ca. 356 Ma) as the time of fabric formation is more appropriate. If so, this deformation would correspond to an episode of ~NE–SW contraction in the earliest Carboniferous. This time constraint is supported by the fact that foliated Ordovician–Silurian clasts occur in the basal conglomerate of the Lower Carboniferous sequence (Fig. 8H), thus suggesting that the Lower Carboniferous rocks were deposited after the fabric development in the Ordovician–Silurian Ahabulake Group. The constraint is also supported by the observation that non-foliated limestone and siltstone in the lower Ma'anqiao Formation unconformably overlie foliated rocks of the Ahabulake Group (Fig. 8G).

The timing of folding in the Ma'anqiao Formation (above the Ordovician–Silurian Ahabulake Group in Domain 4) is not well constrained. Charvet et al. (2007) inferred that this deformation event likely occurred in the Late Carboniferous in response to an initial stage of collision (see discussion below). The suggestion is supported by the occurrence of an angular unconformity between Permian sedimentary rocks and the folded rocks of the Ma'anqiao Formation (Figs. 2 and 3) (BGMRX, 1959).

South Tianshan Belt

Based on zircon U-Pb geochronology, gneissic granitoids in the South Tianshan Belt (Domain 6) were emplaced at 407–396 Ma (Yang and Wang, 2006; Chen et al., 2015). These zircon ages are considerably older than our monazite U-Pb ages of 303–299 Ma from sheared schists and gneisses. Hornblende, muscovite and biotite $^{40}Ar/^{39}Ar$ ages from granitic gneiss, mica schist and amphibolite are 298–293 Ma (Figs. 13A–13E). These new $^{40}Ar/^{39}Ar$ ages overlap with published $^{40}Ar/^{39}Ar$ ages (302.4 ± 8.9 Ma for hornblende; 299.6 ± 1.3 and 298.9 ± 1.2 Ma for muscovite; 292.8 ± 0.9 and 287.8 ± 0.8 Ma for biotite) from granitic gneiss in the South Tianshan Belt (Yang et al., 2007). A slightly older $^{40}Ar/^{39}Ar$ biotite age of 311.9 ± 1.7 Ma was also reported by Yang et al. (2007), but this age is characterized by a hump-shaped spectra and is at odds with a 292.8 ± 0.9 Ma $^{40}Ar/^{39}Ar$ biotite age from the same site. Overall, mylonitic rocks in the South Tianshan Belt contain 303–299 Ma monazite grains that are slightly older than the hornblende, muscovite, and biotite $^{40}Ar/^{39}Ar$ ages.

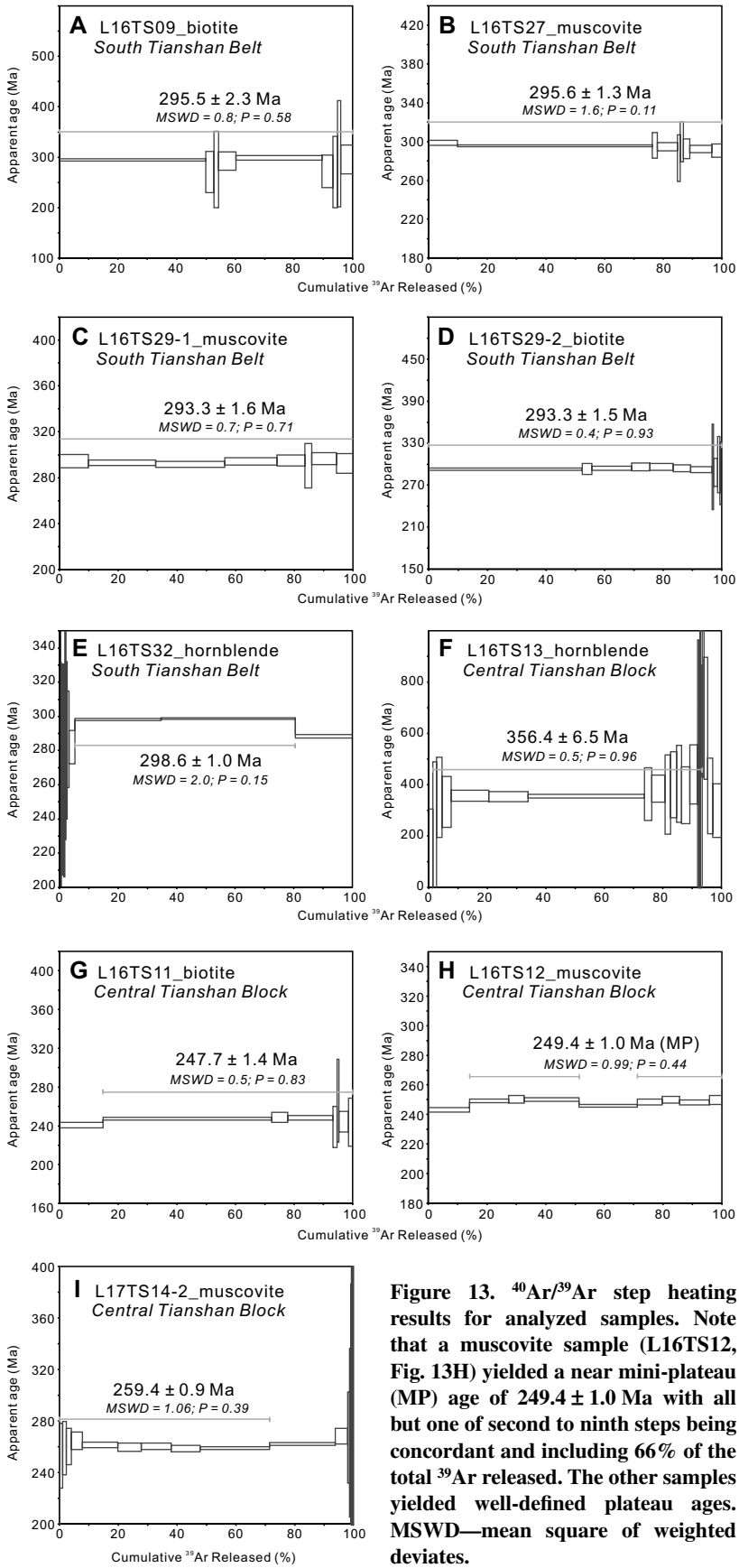

Figure 13. $^{40}Ar/^{39}Ar$ step heating results for analyzed samples. Note that a muscovite sample (L16TS12, Fig. 13H) yielded a near mini-plateau (MP) age of 249.4 ± 1.0 Ma with all but one of second to ninth steps being concordant and including 66% of the total ^{39}Ar released. The other samples yielded well-defined plateau ages. MSWD—mean square of weighted deviates.

The monazite ages could either represent the timing of top-to-ESE shearing, or a pre-shearing deformation/metamorphic event.

The dynamically recrystallized quartz associated with shearing shows irregular shape and lobate contacts (Fig. 11H), indicating recrystallization in high temperatures (>500 °C) through grain boundary migration (Stipp et al., 2002). The assignment of a high crystallization temperature is further supported by the presence of chessboard extinction of quartz (Fig. 11G), which is generated by the α-β transformation (>630 °C) in quartz (Kruhl, 1996; Stipp et al., 2002). Given that monazite could have been crystallized during low-grade metamorphism (<440 °C) (Janots et al., 2008) and the top-to-ESE deformation temperature reached 630 °C, we think that it is more likely that the 303–299 Ma monazite age represents the timing of top-to-ESE shearing. The 298–293 Ma $^{40}Ar/^{39}Ar$ ages represent the timing of cooling in the South Tianshan Belt below the closure temperature of dated minerals (585 ± 50 °C for hornblende, 425 ± 70 °C for muscovite, and 365 ± 35 °C for biotite) (Scibiorski et al., 2015), which could have been driven by continuous top-to-ESE shearing. These $^{40}Ar/^{39}Ar$ ages could also provide a maximum constraint for the timing of macroscopic folds in the South Tianshan Belt.

A series of mafic dikes crosscut the macroscopic folds in the South Tianshan Belt (Domain 6; Fig. 10) and the Central Tianshan Block (Domain 4; Fig. 7). One of these dikes yielded a whole-rock $^{40}Ar/^{39}Ar$ isochron age of 194.3 ± 0.6 Ma (Zhou et al., 2008). This age is likely a mixture between the age of alteration and the true crystallization age, as commonly observed in whole-rock $^{40}Ar/^{39}Ar$ analyses of mafic rocks (e.g., Hofmann et al., 2000; Jourdan et al., 2012). The age, therefore, provides a strict minimum constraint on the timing of folding in the South Tianshan Belt and Central Tianshan Block.

Structural Evolution of the Chinese Tianshan Orogen along the Gangou Section

Our structural observations show variable deformation styles across the North Tianshan Belt, the Central Tianshan Block, and the South Tianshan Belt. Here we summarize the structural history based on our observations and the geochronological constraints. We use $D_{N1–2}$, $D_{C1–4}$ and $D_{S1–2}$ to refer to episodes of deformation in the North Tianshan Belt, Central Tianshan Block, and South Tianshan Belt, respectively. In order to avoid repetition, we discuss dextral shear deformation only in the context of the Central Tianshan Block, even

though this deformation also affected the margins of the North Tianshan Belt and South Tianshan Belt.

North Tianshan Belt

Deformation in the North Tianshan Belt involved mainly two generations of structures. The first phase of deformation (D_{N1}) is associated with mesoscopic and macroscopic upright to inclined folds. These structures, which are recognized in most parts of the North Tianshan Belt (Domains 2 and 3; Fig. 4), are indicative of subhorizontal ~NE–SW shortening during or after the latest Carboniferous. Deformation was characterized by an increase in shortening strain toward the south, as indicated by the occurrence of axial plane foliation within the Yamansu Formation in the southern North Tianshan Belt (Fig. 4). A second phase of deformation (D_{N2}), which took place during the Cenozoic, was responsible for folding and northeastward thrusting along the northern margin of the North Tianshan Belt (Domain 1; Fig. 4). Overprinting relationships between D_{N1} and D_{N2} structures are rarely recognized. A reverse fault with NE-directed movement, which crosscuts the mylonitic fabric of the dextral Main Tianshan Shear Zone (Fig. 6G), may correspond to the D_{N2} phase of deformation.

Central Tianshan Block

Four phases of deformation are recognized in the Central Tianshan Block (D_{C1}–D_{C4}). The earliest deformation (D_{C1}), constrained to the Early Devonian (ca. 399 Ma), involved sinistral strike-slip shearing along the South Central Tianshan Shear Zone (Domain 5; Fig. 7). Subsequent deformation (D_{C2}) is represented by the occurrence of a penetrative axial-planar foliation in the Ahabulake Group (Domain 4; Fig. 7). This deformation, which is constrained to ca. 356 Ma (hornblende $^{40}Ar/^{39}Ar$ age from the Ahabulake Group), was associated with subhorizontal ~NE–SW shortening, and was followed by the deposition of the Ma'anqiao Formation. A later phase of ~NE–SW shortening (D_{C3}), in the Late Carboniferous, was responsible for folding the Lower Carboniferous Ma'anqiao Formation and the development of a spaced axial plane foliation. The effect of D_{C3} on the earlier structures (D_{C1} and D_{C2}) are not well constrained, but we consider that D_{C3} did not significantly modify the orientation of earlier structures because there is no evidence that late folding affected D_{C1} and D_{C2}. Therefore, we think that the subvertical fabric (D_{C1} and D_{C2}) likely represents the original orientation.

Dextral strike-slip deformation (D_{C4}) affected the whole Central Tianshan Block. This deformation occurred mainly along the northern and southern margin of the Central Tianshan Block (Fig. 7), and likely led to the juxtaposition of rocks from different crustal levels in Domains 4 and 5. The timing of D_{C4} deformation is constrained to 290–244 Ma by $^{40}Ar/^{39}Ar$ dating (Laurent-Charvet et al., 2003; Yang et al., 2009; Cai et al., 2012 and this study).

South Tianshan Belt

Two phases of deformation are recorded in the South Tianshan Belt (Domain 6). The earlier deformation (D_{S1}), ca. 303–299 Ma by monazite U-Pb and $^{40}Ar/^{39}Ar$ ages (Figs. 12C–12E and 13A–13E), produced top-to-ESE shear fabric and ~WNW–ESE stretching lineation. This fabric was affected by a later deformation (D_{S2}) associated with macroscopic ~E–W folds (Fig. 10). The gentle inter-limb angle of the ~E–W folds, and the lack of an axial plane fabric, indicate that the strain during D_{S2} was relatively low.

Tectonic Implications

The evidence of polyphase deformation along the Gangou section (Fig. 14) provides constraints on the tectonic evolution of the Chinese Tianshan Orogen, and allows us to highlight potential mechanisms that could be tested in future studies.

Early Devonian Oblique Subduction

Sinistral shearing in the Central Tianshan Block (D_{C1}), at ca. 399 Ma, was contemporaneous with widespread arc-related magmatism (Gao et al., 2009; Dong et al., 2011; Lin et al., 2013; Ge et al., 2014; Ma et al., 2014; Chen et al., 2015; Han and Zhao, 2018). Therefore, it is likely that sinistral shearing was associated with an episode of oblique subduction in the Early Devonian.

The Central Tianshan Block was likely connected to the northern Tarim Craton in the early Paleozoic (Shu et al., 1999; Gao et al., 2009; Lin et al., 2009; Charvet et al., 2011; Wang et al., 2011; Han et al., 2016a). This is indicated by similar detrital zircon age populations in the Neoproterozoic to early Paleozoic strata, and the occurrence of common Ordovician–Silurian conodont and brachiopod species in both the northern Tarim Craton and the Central Tianshan Block (Rong et al., 1995; Wang et al., 2007c; Ma et al., 2012; Han et al., 2015). The separation of the Central Tianshan Block from the Tarim Craton may have initiated in the middle Paleozoic, as demonstrated by the occurrence of 423–309 Ma ophiolites in the South Tianshan Belt (Han et al., 2015 and references therein; Wang et al., 2018) and the transition from shallow to deep marine deposition in the South Tianshan Belt during the Silurian–Devonian (Wu and Li, 2013). The combination of deep marine sedimentation and ophiolitic material may indicate that a back-arc basin developed along the South Tianshan Belt. In the South Tianshan Belt and the Central Tianshan Block, a remarkable shift of zircon εHf(t) toward positive values since ca. 400 Ma is indicative of a decreasing crustal contribution during magma generation (Zhang et al., 2016; Han et al., 2016a), which likely corresponds to an episode of crustal thinning (Kemp et al., 2009; Collins et al., 2011). According to Han et al. (2015; 2016a) and Zhang et al. (2016), the middle Paleozoic separation of the Central Tianshan Block and the opening of the South Tianshan back-arc basin may have been driven by trench retreat, similarly to the development of the Japan Sea. If the sinistral strike-slip deformation indeed operated simultaneously with the opening of the back-arc basin, this would indicate an episode of oblique trench retreat in the Early Devonian (Fig. 15). Alternatively, sinistral shearing may have occurred in response to a short episode of oblique subduction, unrelated to the opening of the South Tianshan back-arc basin.

The role of strike-slip deformation has been discussed widely in the context of the tectonic evolution of the Central Asian Orogenic Belt. Şengör et al. (1993) and Şengör and Natal'in (1996) have suggested that the earlier arc system was laterally cut and displaced by a series of syn/post-subduction strike-slip faults to form a map-view duplex of magmatic arcs. Other authors proposed that strike-slip shear zones were linked to lateral migration of orogenic materials following the amalgamation of the Siberian, Baltic, Tarim, and North China cratons (e.g., Laurent-Charvet et al., 2003; Wang et al., 2007a; Choulet et al., 2013). Our observations suggest that strike-slip movement occurred parallel to the subduction zone. Oblique plate convergence is a common feature in plate tectonics (Díaz-Azpiroz et al., 2016), and we therefore think that the evidence of sinistral strike-slip deformation (D_{C1}) highlights the role of oblique subduction in the buildup of the Tianshan Orogen.

Early Carboniferous Contractional Deformation

In the earliest Carboniferous (ca. 356 Ma), the Central Tianshan Block underwent contractional deformation as demonstrated by folds and penetrative axial plane foliations in the Ahabulake Group (D_{C2}; Fig. 7). This contractional event is also recorded in the South Tianshan Belt (Heiyingshan area, Fig. 14), which experienced northward ductile thrusting at 359–356 Ma ($^{40}Ar/^{39}Ar$ plateau ages of syn-deformation muscovite; Wang et al., 2011). An angular unconformity below the Lower Carboniferous sedimentary rocks

(e.g., the Ma'anqiao Formation) may mark the termination of this contractional deformation (Shu et al., 2002). Wang et al. (2011) suggested that this contractional event was associated with the collision of the Tarim Craton with the Central Tianshan Block. However, it has recently been suggested that the collision took place in the latest Carboniferous (e.g., Han and Zhao, 2018). We therefore propose that the Early Carboniferous contractional deformation was likely associated with southward trench advance that induced overriding-plate compression and led to inversion of the South Tianshan back-arc basin (Fig. 15).

Trench migration is arguably one of the major mechanisms that control the tectonic evolution of accretionary orogens (Royden, 1993; Schellart et al., 2007; Rosenbaum and Mo, 2011). For example, in the Tasmanides (eastern Australia), episodic trench retreat and advance led to the opening and inversion of multiple back-arc basins, thus contributing to the lateral growth of the orogenic system (Collins, 2002; Rosenbaum, 2018). The large orogenic width of the Central Asian Orogenic Belt might have resulted from similar processes (Xiao et al., 2018).

Latest Carboniferous to Permian Collisional Orogeny

The Chinese Tianshan Orogen evolved into a collisional phase in the latest Paleozoic, following the closure of the southern branch of the Paleo-Asian Ocean (e.g., Han and Zhao, 2018). It remains controversial, however, when exactly this ocean was consumed, with previous suggestions ranging from Late Devonian to earliest Triassic (Han et al., 2011, and references therein). Based on the following lines of evidence, Han and Zhao (2018) have recently proposed that the final ocean closure and the associated collision took place during the latest Carboniferous (<310 Ma). First, the occurrence of 321–309 Ma ophiolites in the middle and eastern segments of the South Tianshan Belt indicates that oceanic crust was still produced in the Late Carboniferous (Han and Zhao, 2018; Wang et al., 2018, and references therein). Second, the abrupt decrease in the values of εHf(t) in magmatic zircon younger than 310 Ma is indicative of an increasing contribution of radiogenic crustal material; this might correspond to the transition from subduction to collision (Han et al., 2016b; Han and Zhao, 2018). Third, a major angular unconformity between Devonian and Upper Carboniferous rocks in the Tarim Basin (Carroll et al., 2001) might have formed in response to this collision.

Farther north, the timing of collision between the island arc system of the North Tianshan Belt (e.g., Bogda and Dananhu arcs, Fig. 1) and the Central Tianshan Block is also latest Carboniferous (i.e., simultaneously with the collision between the Tarim Craton and the Central Tianshan Block). Evidence supporting this collision includes the following. (1) Magmatism in the North Tianshan Belt (Eastern Tianshan) changed from calc-alkaline (during the Late Carboniferous) to bimodal (during the Permian) (e.g., Chen et al., 2011; Wang et al., 2014a), and ~305–301 Ma mafic magmatism was characterized by the significant input of sub-slab asthenospheric mantle that was likely induced by slab breakoff (Zhang et al., 2020). (2) The tectonic boundary between the Central Tianshan Block and the North Tianshan island arcs is marked by strike-slip faults (e.g. the Main Tianshan Shear Zone, Figs. 1 and 14), which were active during the Permian (Shu et al., 1999; Laurent-Charvet et al., 2002; Shu et al., 2002; Wang et al., 2008, 2014a). Collision between the two tectonic units must have occurred prior to or during strike-slip deformation. (3) Early Permian sedimentary rocks from the North Tianshan Belt in the Eastern Tianshan contain abundant Precambrian detrital zircon grains that were likely sourced from the Central Tianshan Block (Zhang et al., 2016), thus implying that the amalgamation of the North Tianshan island arc system and the Central Tianshan Block occurred prior to the Permian.

Along the Gangou section, the structural response to the initial collision of the Central Tianshan Block with the Tarim Craton and the

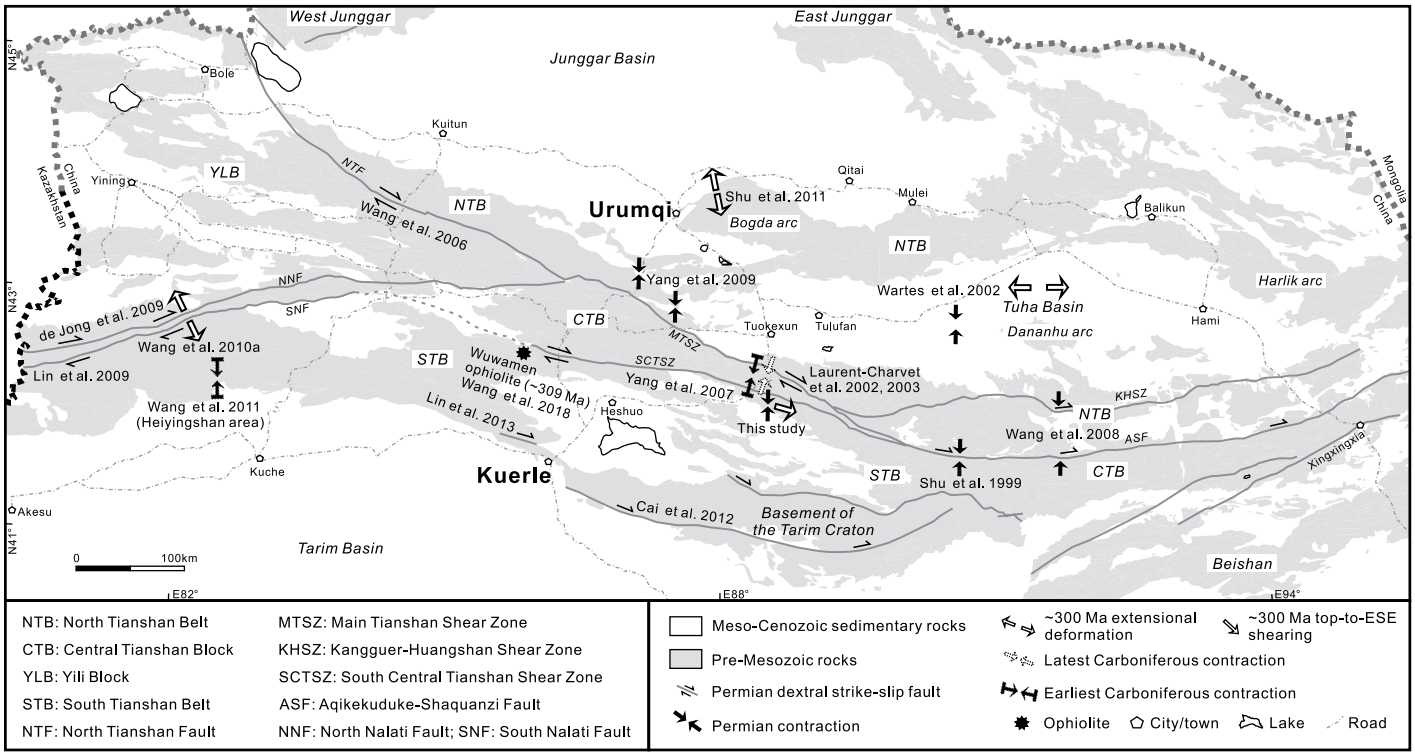

Figure 14. Major Carboniferous to Permian structures in the Chinese Tianshan Orogen. The data compilation incorporates structures, for which the timing of deformation is relatively well constrained.

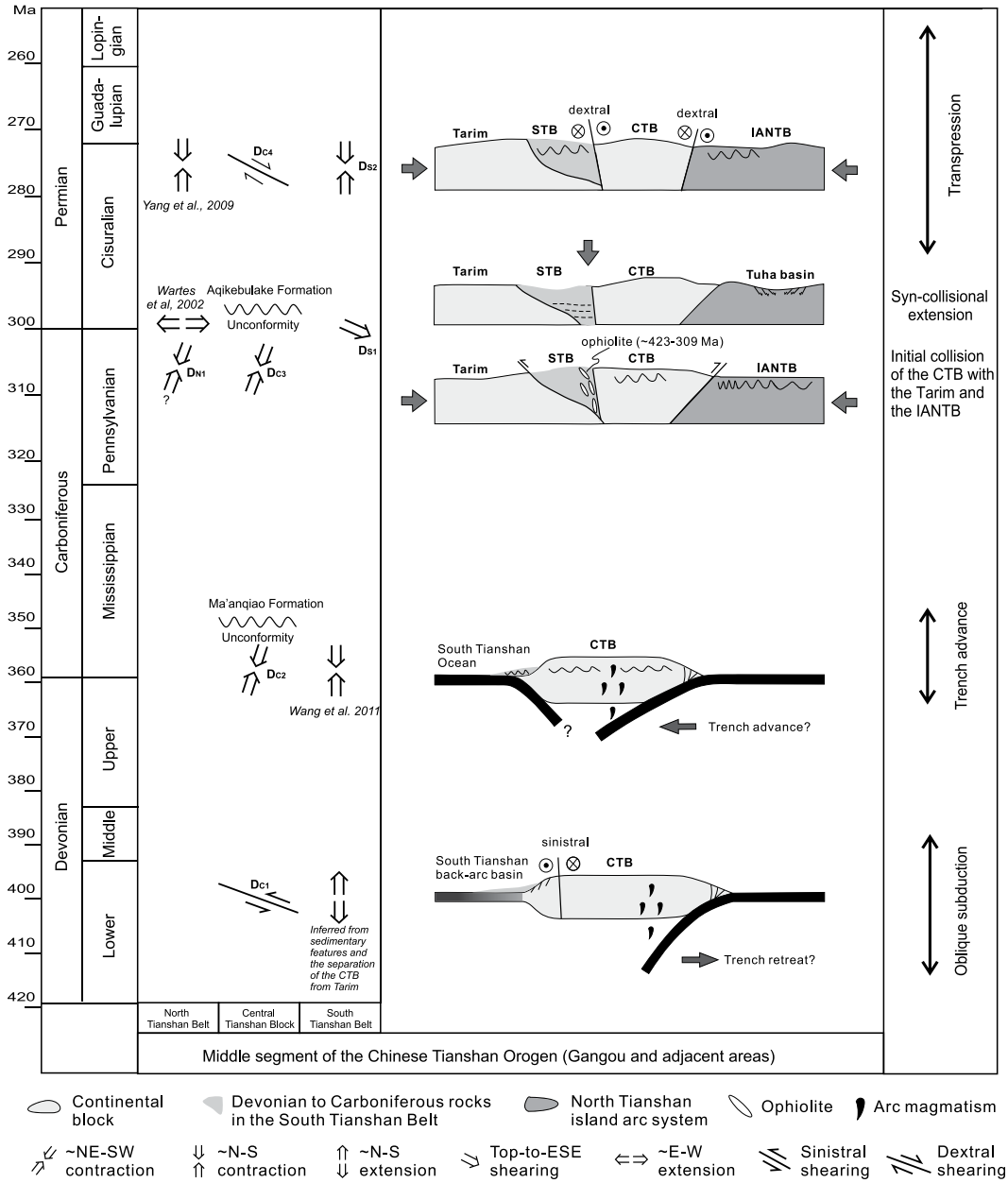

Figure 15. Schematic illustration of the late Paleozoic tectonic evolution of the middle segment of the Chinese Tianshan Orogen (Gangou section and adjacent areas). Devonian arc magmatism is based on Chen et al. (2015) and Dong et al. (2011). CTB—Central Tianshan Block; STB—South Tianshan Belt; IANTB—island arc system of the North Tianshan Belt.

Northern Tianshan island arc system, is not well constrained. Our results indicate that ~NW–SE folds (D_{C3}) in the Central Tianshan Block (Domain 4) occurred during the Late Carboniferous. This deformation might have been triggered by the initial collision. Carboniferous rocks in the North Tianshan Belt, which belong to the Northern Tianshan island arc system (Fig. 2), also record ~NE–SW shortening deformation (D_{N1}), which must have occurred during or after the Late Carboniferous. The progressive increase of ~NE–SW shortening strain toward the south supports the suggestion that this deformation was linked to the initial collision of the North Tianshan Belt with the Central Tianshan Block along the Main Tianshan Shear Zone.

Following the initial collision, the South Tianshan Belt experienced a phase of top-to-ESE shear deformation (D_{S1}) dated at ca. 300 Ma. The role that this deformation played in the evolution of the orogen remains enigmatic. The fact that D_{S2} fold axial planes are steeply dipping and the hinges are shallowly plunging to the ESE (subparallel to D_{S1} stretching lineation and the orogenic strike, Fig. 10) suggests that (1) the original dip of the D_{S1} mylonitic foliation was shallow, and (2) the original orientation of the D_{S1} stretching lineation was parallel to the orogen. Such fabrics could have been formed in response to extensional deformation. Extensional structures, dated at ca. 300 Ma, have been reported in the adjacent Tuha Basin and in the area of the Bogda arc in the Eastern Tianshan (Figs. 1 and 14) (Wartes et al., 2002; Shu et al., 2011). In the Western Tianshan, south-directed normal faulting occurred simultaneously with high-temperature metamorphism at ca. 299 Ma (Li and Zhang, 2004; Wang et al., 2010a) and widespread felsic magmatism at ca. 300 Ma (Tang et al., 2017). This evidence for extensional deformation and associated thermal pulse supports the suggestion that the D_{S1} deformation in the Gangou section was linked to a phase of (syn- or post-orogenic) orogen-parallel extension. Similar types of orogen-parallel extensional structures are widely recognized in other collisional orogens, such as the eastern Alps and

the Himalayas (e.g., Scharf et al., 2013; Xu et al., 2013). The occurrence of the shallowly dipping foliation and orogen-parallel stretching lineation indicates an overall flow parallel to the strike of the orogen, which could have been driven via gravitational collapse or by a lateral tectonic escape (Brun et al., 1985; Dewey, 1988; Frisch et al., 2000; Selverstone, 2005; Duclaux et al., 2007; Scharf et al., 2013; Xu et al., 2013).

Dextral strike-slip shearing (D_{C4}) in the Chinese Tianshan Orogen commenced at ca. 290 Ma as discussed above and was mainly localized at the margins of the Central Tianshan Block (i.e., Main Tianshan Shear Zone and South Central Tianshan Shear Zone; Fig. 14). These shear zones are connected to the ~E–W Kangguer-Huangshan Shear Zone and the Aqikekudukе-Shaquanzi Fault (Eastern Tianshan, Fig. 14), with the latter showing evidence of transpressional deformation in the form of positive flower structures (Shu et al., 1999; Wang et al., 2008). In the Gangou section, dextral shearing was coeval with the development of ~E–W folds in the North Tianshan Belt at ca. 266 Ma (Fig. 14; Yang et al., 2009) and ~E–W folds in the South Tianshan Belt (D_{S2}) at 293–194 Ma (Fig. 14). The ~NW–SE orientation of the dextral shear zones is oblique to ~E–W folds in the North Tianshan Belt and South Tianshan Belt (Fig. 14), suggesting partitioning of the Permian transpressional deformation into fold domains (D_{S2}) and discrete shear zones (D_{C4}).

In a summary, latest Carboniferous to Permian collisional orogeny in the middle segment of the Chinese Tianshan Orogen involved contractional, extensional, and transpressional deformation. Similar processes have been recognized elsewhere in the western Central Asian Orogenic Belt. For example, the Late Carboniferous to Permian collision of the Chinese Altai with the East/West Junggar (along the Irtysh Shear Zone) might have involved an initial stage of crustal thickening, followed by orogen-parallel extension and transpressional deformation (Li et al., 2015, 2017).

Cenozoic Reactivation of the Chinese Tianshan Orogen

In the Meso-Cenozoic, uplift and deformation occurred in the Central Asian Orogenic Belt in response to the far-field stresses transmitted from the southern margin of Asia and the India–Asia collision (Dumitru et al., 2001; Jolivet et al., 2010; Gillespie et al., 2017; Yin et al., 2018). Our observations from the Gangou section show evidence for Cenozoic folds and thrusts (D_{N2}, Figs. 2 and 4). The fact that mafic dikes (≥194 Ma as discussed above) in the Central Tianshan Block and the South Tianshan Belt are undeformed (Figs. 7 and 11), indicates that Meso–Cenozoic shortening deformation was partitioned and mainly accommodated along thrusts at the mountain foot. These thrusts were responsible for shaping the present-day landscape, overthrusting the Tianshan Orogen on top of the Tarim Craton in the south and the Junggar Basin in the north (e.g., Avouac et al., 1993; Sobel and Dumitru, 1997; Wang et al., 2004). This phase of intracontinental deformation has also reactivated Paleozoic faults, as shown by the evidence of brittle thrusting in the Main Tianshan Shear Zone (Fig. 6G).

CONCLUSIONS

The Gangou section in the Chinese Tianshan Orogen shows evidence of Devonian to Cenozoic polyphase deformation. In the North Tianshan Belt, two generations of structures were recognized, associated with syn-/post–Late Carboniferous ~NW–SE folds and reverse faults (D_{N1}) and Cenozoic northward thrusting (D_{N2}). Farther south, in the Central Tianshan Block, we found evidence for four phases of deformation ($D_{C1–4}$). D_{C1} represents Early Devonian sinistral shearing; D_{C2} and D_{C3} involved ~NE–SW shortening in the earliest Carboniferous and Late Carboniferous, respectively; and D_{C4} involved dextral strike-slip deformation during the Permian, which was focused along the northern and southern margins of the Central Tianshan Block. In the South Tianshan Belt, ca. 300 Ma top-to-ESE shear fabric (D_{S1}) was subsequently overprinted by ~E–W folds (D_{S2}).

Based on the structural observations, the following tectonic history is inferred. During the Early Devonian, oblique subduction might have affected the Chinese Tianshan Orogen, as demonstrated by orogen-parallel sinistral shearing (D_{C1}). During the earliest Carboniferous, orogen-perpendicular contraction (D_{C2}) was possibly driven by an episode of trench advance. The collision of the Central Tianshan Block with the Tarim Craton and the North Tianshan island arc system in the Latest Carboniferous to Permian possibly controlled orogen-perpendicular contraction (D_{C3} and D_{N1}), orogen-parallel extension (D_{S1}), and transpressional deformation (D_{C4} and D_{S2}). Far-field stresses transmitted from the plate boundary were responsible for Cenozoic reactivation of the Chinese Tianshan Orogen and thrusting along the mountain foot (D_{N2}).

ACKNOWLEDGMENTS

This study was financially supported by the National Key Research & Development Program of China (Grant No. 2017YFC0601205), National Science Foundation China (41872222), the international partnership program of the Chinese Academy of Sciences (Grant No. 132744KYSB20190039), and Hong Kong Research Grant Council (HKU 17302317 and HKU17303415). P. Li is supported by the Thousand Youth Talents Plan, and a project from Guangdong Province (2019QN01H101). Y. Jiang acknowledges the Guangdong Special Support Program. We thank Weifeng Xiao for discussing Tianshan geology, Wanwan Hu, Xiangsong Wang and Yannan Wang for field assistance, and Chutian Shu for assisting with one of the illustrations. This is a contribution of Guangzhou Institute of Geochemistry, Chinese Academy of Sciences (GIGCAS; No. IS-2820), the Chemical Geodynamics Joint Laboratory between Hong Kong University and GIG (CAS) as well as International Geoscience Programme (IGCP) 662.

REFERENCES CITED

Abrajevitch, A., Van der Voo, R., Bazhenov, M.L., Levashova, N.M., and McCausland, P.J.A., 2008, The role of the Kazakhstan orocline in the late Paleozoic amalgamation of Eurasia: Tectonophysics, v. 455, no. 1–4, p. 61–76, https://doi.org/10.1016/j.tecto.2008.05.006.

Alexeiev, D.V., Biske, Y.S., Wang, B., Djenchuraeva, A.V., Getman, O.F., Aristov, V.A., Kröner, A., Liu, H., and Zhong, L., 2015, Tectono-stratigraphic framework and Palaeozoic evolution of the Chinese South Tianshan: Geotectonics, v. 49, no. 2, p. 93–122, https://doi.org/10.1134/S0016852115020028.

Alexeiev, D.V., Kröner, A., Hegner, E., Rojas-Agramonte, Y., Biske, Y.S., Wong, J., Geng, H., Ivleva, E., Mühlberg, M., and Mikolaichuk, A., 2016, Middle to Late Ordovician arc system in the Kyrgyz Middle Tianshan: From arc-continent collision to subsequent evolution of a Palaeozoic continental margin: Gondwana Research, v. 39, p. 261–291, https://doi.org/10.1016/j.gr.2016.02.003.

Allen, M.B., Windley, B.F., and Zhang, C., 1993a, Palaeozoic collisional tectonics and magmatism of the Chinese Tien Shan, central Asia: Tectonophysics, v. 220, no. 1, p. 89–115, https://doi.org/10.1016/0040-1951(93)90225-9.

Allen, M.B., Windley, B.F., Zhang, C., and Guo, J., 1993b, Evolution of the Turfan Basin, Chinese central Asia: Tectonics, v. 12, no. 4, p. 889–896, https://doi.org/10.1029/93TC00598.

Allen, M.B., Şengör, A.M.C., and Natal'in, B.A., 1995, Junggar, Turfan and Alakol basins as Late Permian to ?Early Triassic extensional structures in a sinistral shear zone in the Altaid orogenic collage, Central Asia: Journal of the Geological Society, v. 152, no. 2, p. 327–338, https://doi.org/10.1144/gsjgs.152.2.0327.

Amante, C., and Eakins, B.W., 2009, ETOPO1 1 arc-minute global relief model: procedures, data sources and analysis, NOAA Technical Memorandum NESDIS NGDC-24, 19 p., https://www.ngdc.noaa.gov/mgg/global/relief/ETOPO1/docs/ETOPO1.pdf (accessed February 2020).

An, F., Zhu, Y., Wei, S., and Lai, S., 2017, The zircon U-Pb and Hf isotope constraints on the basement nature and Paleozoic evolution in northern margin of Yili Block, NW China: Gondwana Research, v. 43, p. 41–54, https://doi.org/10.1016/j.gr.2015.11.014.

Avouac, J.P., Tapponnier, P., Bai, M., You, H., and Wang, G., 1993, Active thrusting and folding along the northern Tien Shan and Late Cenozoic rotation of the Tarim relative to Dzungaria and Kazakhstan: Journal of Geophysical Research. Solid Earth, v. 98, no. B4, p. 6755–6804, https://doi.org/10.1029/92JB01963.

BGMRX, 1959, Geological map and explanatory note of the Kumishi sheet: Bureau of Geology and Mineral Resources of Xinjiang, Government Printer, Map K-45-XVII, scale 1:200,000.

BGMRX, 1993, Bureau of Geology and Mineral Resources of Xinjiang Autonomous Region, Regional Geology of Xinjiang Autonomous Region: Beijing, Geological Publishing House, 841 p. (in Chinese with English abstract).

Biske, Y.S., and Seltmann, R., 2010, Paleozoic Tian-Shan as a transitional region between the Rheic and

Urals-Turkestan oceans: Gondwana Research, v. 17, no. 2, p. 602–613, https://doi.org/10.1016/j.gr.2009.11.014.

Brookfield, M., 2000, Geological development and Phanerozoic crustal accretion in the western segment of the southern Tien Shan (Kyrgyzstan, Uzbekistan and Tajikistan): Tectonophysics, v. 328, no. 1, p. 1–14, https://doi.org/10.1016/S0040-1951(00)00175-X.

Brun, J.P., Burg, J.P., and Ming, C.G., 1985, Strain trajectories above the Main Central Thrust (Himalaya) in southern Tibet: Nature, v. 313, no. 6001, p. 388–390, https://doi.org/10.1038/313388a0.

Burtman, V., 2006, The Tien Shan early Paleozoic tectonics and geodynamics: Russian Journal of Earth Sciences, v. 8, no. 3, p. 1–23, https://doi.org/10.2205/2006ES000202.

Cai, Z., Xu, Z., He, B., and Wang, R., 2012, Age and tectonic evolution of ductile shear zones in the eastern Tianshan-Beishan orogenic belt: Acta Petrologica Sinica, v. 28, no. 6, p. 1875–1895 (in Chinese with the English abstract).

Carroll, A.R., Graham, S.A., Chang, E.Z., and McKnight, C., 2001, Sinian through Permian tectonostratigraphic evolution of the northwestern Tarim basin, China, *in* Hendrix, M.S., and Davis, G.A., eds., Paleozoic and Mesozoic Tectonic Evolution of Central and Eastern Asia: From Continental Assembly to Intracontinental Deformation: Geological Society of America Memoir 194, p. 47–70, https://doi.org/10.1130/0-8137-1194-0.47.

Cawood, P.A., and Hawkesworth, C.J., 2015, Temporal relations between mineral deposits and global tectonic cycles, *in* Jenkin, G.R.T., Lusty, P.A.J., McDonald, I., Smith, M.P., Boyce, A.J., and Wilkinson, J.J., eds., Ore Deposits in an Evolving Earth: Geological Society of London Special Publication 393, p. 9–21, https://doi.org/10.1144/SP393.1.

Cawood, P.A., Kröner, A., Collins, W.J., Kusky, T.M., Mooney, W.D., and Windley, B.F., 2009, Accretionary orogens through Earth history, *in* Cawood, P.A., and Kröner, A., eds., Earth Accretionary Systems in Space and Time, Geological Society of London Special Publications 318, p. 1–36, https://doi.org/10.1144/SP318.1.

Charvet, J., Shu, L.S., and Laurent-Charvet, S., 2007, Paleozoic structural and geodynamic evolution of eastern Tianshan (NW China): welding of the Tarim and Junggar plates: Episodes, v. 30, no. 3, p. 162–186.

Charvet, J., Shu, L., Laurent-Charvet, S., Wang, B., Faure, M., Cluzel, D., Chen, Y., and Jong, K., 2011, Palaeozoic tectonic evolution of the Tianshan belt, NW China: Science China. Earth Sciences, v. 54, no. 2, p. 166–184, https://doi.org/10.1007/s11430-010-4138-1.

Chen, B., Long, X., Yuan, C., Wang, Y., Sun, M., Xiao, W., Cai, K., and Huang, Z., 2015, Geochronology and geochemistry of Late Ordovician–Early Devonian gneissic granites in the Kumishi area, northern margin of the South Tianshan Belt: Constraints on subduction process of the South Tianshan Ocean: Journal of Asian Earth Sciences, v. 113, p. 293–309, https://doi.org/10.1016/j.jseaes.2014.09.034.

Chen, C., Lu, H., Jia, D., Cai, D., and Wu, S., 1999, Closing history of the southern Tianshan oceanic basin, western China: an oblique collisional orogeny: Tectonophysics, v. 302, no. 1, p. 23–40, https://doi.org/10.1016/S0040-1951(98)00273-X.

Chen, C., Lü, X.B., Cao, X.F., Wu, C.M., and Zhu, J., 2013, Geochronology, geochemistry and geological significance of Late Carboniferous-Early Permian granites in Kumishi area, Xinjiang: Earth Science, v. 38, no. 2, p. 218–232 (in Chinese with the English abstract).

Chen, X., Shu, L., and Santosh, M., 2011, Late Paleozoic post-collisional magmatism in the Eastern Tianshan Belt, Northwest China: New insights from geochemistry, geochronology and petrology of bimodal volcanic rocks: Lithos, v. 127, no. 3, p. 581–598, https://doi.org/10.1016/j.lithos.2011.06.008.

Choulet, F., Chen, Y., Cogné, J.-P., Rabillard, A., Wang, B., Lin, W., Faure, M., and Cluzel, D., 2013, First Triassic palaeomagnetic constraints from Junggar (NW China) and their implications for the Mesozoic tectonics in Central Asia: Journal of Asian Earth Sciences, v. 78, p. 371–394, https://doi.org/10.1016/j.jseaes.2013.01.023.

Collins, W.J., 2002, Hot orogens, tectonic switching, and creation of continental crust: Geology, v. 30, no. 6, p. 535–538, https://doi.org/10.1130/0091-7613(2002)030<0535:HOTSAC>2.0.CO;2.

Collins, W.J., Belousova, E.A., Kemp, A.I.S., and Murphy, J.B., 2011, Two contrasting Phanerozoic orogenic systems revealed by hafnium isotope data: Nature Geoscience, v. 4, no. 5, p. 333–337, https://doi.org/10.1038/ngeo1127.

Díaz-Azpiroz, M., Brune, S., Leever, K.A., Fernández, C., and Czeck, D.M., 2016, Tectonics of oblique plate boundary systems: Tectonophysics, v. 693, p. 165–170, https://doi.org/10.1016/j.tecto.2016.07.028.

de Jong, K., Wang, B., Faure, M., Shu, L., Cluzel, D., Charvet, J., Ruffet, G., and Chen, Y., 2009, New $^{40}Ar/^{39}Ar$ age constraints on the Late Palaeozoic tectonic evolution of the western Tianshan (Xinjiang, northwestern China), with emphasis on Permian fluid ingress: International Journal of Earth Sciences, v. 98, no. 6, p. 1239–1258, https://doi.org/10.1007/s00531-008-0338-8.

Degtyarev, K., Yakubchuk, A., Tretyakov, A., Kotov, A., and Kovach, V., 2017, Precambrian geology of the Kazakh uplands and Tien Shan: an overview: Gondwana Research, v. 47, p. 44–75, https://doi.org/10.1016/j.gr.2016.12.014.

Demange, M.A., 2012, Mineralogy for Petrologists: Optics, Chemistry, and Occurrences of Rock-forming Minerals: London, UK, CRC Press, 201 p, https://doi.org/10.1201/b12307.

Deng, S.T., Guo, Z.J., Zhang, Z.C., and Liao, G.H., 2006, Timing of the formation of the Sangshuyuanzi ductile shear zone in the central segment of the South Tianshan and its tectonic significance: Geology in China, v. 81, no. 2, p. 641–647 (in Chinese with the English abstract).

Dewey, J.F., 1988, Extensional collapse of orogens: Tectonics, v. 7, no. 6, p. 1123–1139, https://doi.org/10.1029/TC007i006p01123.

Dong, Y.P., Zhou, D.W., Zhang, G.W., Zhao, X., Luo, J.H., and Xu, J.G., 2006, Geology and geochemistry of the Gangou ophiolitic mélange at the northern margin of the Middle Tianshan Belt: Acta Petrologica Sinica, v. 22, no. 1, p. 49–56.

Dong, Y.P., Zhang, G., Neubauer, F., Liu, X., Hauzenberger, C., Zhou, D., and Li, W., 2011, Syn- and post-collisional granitoids in the Central Tianshan orogen: Geochemistry, geochronology and implications for tectonic evolution: Gondwana Research, v. 20, no. 2–3, p. 568–581, https://doi.org/10.1016/j.gr.2011.01.013.

Duclaux, G., Rey, P., Guillot, S., and Ménot, R.-P., 2007, Orogen-parallel flow during continental convergence: Numerical experiments and Archean field examples: Geology, v. 35, no. 8, p. 715–718, https://doi.org/10.1130/G23540A.1.

Dumitru, T.A., Zhou, D., Chang, E.Z., Graham, S.A., Hendrix, M.S., Sobel, E.R., and Carroll, A.R., 2001, Uplift, exhumation, and deformation in the Chinese Tian Shan, *in* Hendrix, M.S., and Davis, G.A., eds., Paleozoic and Mesozoic Tectonic Evolution of Central and Eastern Asia: From Continental Assembly to Intracontinental Deformation: Geological Society of America Memoir 194, p. 71–100, https://doi.org/10.1130/0-8137-1194-0.71.

Frisch, W., Dunkl, I., and Kuhlemann, J., 2000, Post-collisional orogen-parallel large-scale extension in the Eastern Alps: Tectonophysics, v. 327, no. 3–4, p. 239–265, https://doi.org/10.1016/S0040-1951(00)00204-3.

Gao, J., He, G., Li, M., Xiao, X., Tang, Y., Wang, J., and Zhao, M., 1995, The mineralogy, petrology, metamorphic PTDt trajectory and exhumation mechanism of blueschists, south Tianshan, northwestern China: Tectonophysics, v. 250, no. 1, p. 151–168, https://doi.org/10.1016/0040-1951(95)00026-6.

Gao, J., Li, M., Xiao, X., Tang, Y., and He, G., 1998, Paleozoic tectonic evolution of the Tianshan Orogen, northwestern China: Tectonophysics, v. 287, no. 1, p. 213–231, https://doi.org/10.1016/S0040-1951(97)00211-4.

Gao, J., Long, L., Klemd, R., Qian, Q., Liu, D., Xiong, X., Su, W., Liu, W., Wang, Y., and Yang, F., 2009, Tectonic evolution of the South Tianshan orogen and adjacent regions, NW China: geochemical and age constraints of granitoid rocks: International Journal of Earth Sciences, v. 98, no. 6, p. 1221–1238, https://doi.org/10.1007/s00531-008-0370-8.

Ge, R., Zhu, W., Wilde, S.A., He, J., Cui, X., Wang, X., and Bihai, Z., 2014, Neoproterozoic to Paleozoic long-lived accretionary orogeny in the northern Tarim Craton: Tectonics, v. 33, p. 302–329, https://doi.org/10.1002/2013TC003501.

Gillespie, J., Glorie, S., Jepson, G., Zhang, Z.Y., Xiao, W.J., Danišík, M., and Collins, A.S., 2017, Differential exhumation and crustal tilting in the easternmost Tianshan (Xinjiang, China), revealed by low-temperature thermochronology: Tectonics, v. 36, p. 2142–2158, https://doi.org/10.1002/2017TC004574.

Han, B.F., He, G.Q., Wang, X.C., and Guo, Z.J., 2011, Late Carboniferous collision between the Tarim and Kazakhstan–Yili terranes in the western segment of the South Tian Shan Orogen, Central Asia, and implications for the Northern Xinjiang, western China: Earth-Science Reviews, v. 109, no. 3–4, p. 74–93, https://doi.org/10.1016/j.earscirev.2011.09.001.

Han, Y., and Zhao, G., 2018, Final amalgamation of the Tianshan and Junggar orogenic collage in the southwestern Central Asian Orogenic Belt: Constraints on the closure of the Paleo-Asian Ocean: Earth-Science Reviews, v. 186, p. 129–152, https://doi.org/10.1016/j.earscirev.2017.09.012.

Han, Y., Zhao, G., Sun, M., Eizenhöfer, P.R., Hou, W., Zhang, X., Liu, D., Wang, B., and Zhang, G., 2015, Paleozoic accretionary orogenesis in the Paleo-Asian Ocean: Insights from detrital zircons from Silurian to Carboniferous strata at the northwestern margin of the Tarim Craton: Tectonics, v. 34, https://doi.org/10.1002/2014TC003668.

Han, Y., Zhao, G., Cawood, P.A., Sun, M., Eizenhöfer, P.R., Hou, W., Zhang, X., and Liu, Q., 2016a, Tarim and North China cratons linked to northern Gondwana through switching accretionary tectonics and collisional orogenesis: Geology, v. 44, p. 95–98, https://doi.org/10.1130/G37399.1.

Han, Y., Zhao, G., Sun, M., Eizenhöfer, P.R., Hou, W., Zhang, X., Liu, Q., Wang, B., Liu, D., and Xu, B., 2016b, Late Paleozoic subduction and collision processes during the amalgamation of the Central Asian Orogenic Belt along the South Tianshan suture zone: Lithos, v. 246–247, p. 1–12, https://doi.org/10.1016/j.lithos.2015.12.016.

He, J., Zhu, W., Zheng, B., Wu, H., Cui, X., and Lu, Y., 2015, Neoproterozoic diamictite-bearing sedimentary rocks in the northern Yili Block and their constraints on the Precambrian evolution of microcontinents in the Western Central Asian Orogenic Belt: Tectonophysics, v. 665, p. 23–36, https://doi.org/10.1016/j.tecto.2015.09.021.

Hofmann, C., Féraud, G., and Courtillot, V., 2000, $^{40}Ar/^{39}Ar$ dating of mineral separates and whole rocks from the Western Ghats lava pile: further constraints on duration and age of the Deccan traps: Earth and Planetary Science Letters, v. 180, no. 1, p. 13–27, https://doi.org/10.1016/S0012-821X(00)00159-X.

Hu, A., Jahn, B., Zhang, G., Chen, Y., and Zhang, Q., 2000, Crustal evolution and Phanerozoic crustal growth in northern Xinjiang: Nd isotopic evidence. Part I. Isotopic characterization of basement rocks: Tectonophysics, v. 328, no. 1, p. 15–51, https://doi.org/10.1016/S0040-1951(00)00176-1.

Hu, Z., Zhang, W., Liu, Y., Gao, S., Li, M., Zong, K., Chen, H., and Hu, S., 2015, "Wave" Signal-Smoothing and Mercury-Removing Device for Laser Ablation Quadrupole and Multiple Collector ICPMS Analysis: Application to Lead Isotope Analysis: Analytical Chemistry, v. 87, no. 2, p. 1152–1157, https://doi.org/10.1021/ac503749k.

Huang, Z., Long, X., Kröner, A., Yuan, C., Wang, Y., Chen, B., and Zhang, Y., 2015, Neoproterozoic granitic gneisses in the Chinese Central Tianshan Block: Implications for tectonic affinity and Precambrian crustal evolution: Precambrian Research, v. 269, p. 73–89, https://doi.org/10.1016/j.precamres.2015.08.005.

Huang, Z., Long, X., Yuan, C., Sun, M., Wang, Y., Zhang, Y., and Chen, B., 2016, Detrital zircons from Neoproterozoic sedimentary rocks in the Yili Block: constraints on the affinity of microcontinents in the southern Central Asian Orogenic Belt: Gondwana Research, v. 37, p. 39–52, https://doi.org/10.1016/j.gr.2016.05.009.

Jahn, B.-M., 2004, The Central Asian Orogenic Belt and growth of the continental crust in the Phanerozoic, *in* Malpas, J., et al., eds., Aspects of the Tectonic Evolution in China: Geological Society of London, Special Publications, v. 226, no. 1, p. 73–100, https://doi.org/10.1144/GSL.SP.2004.226.01.05.

Janots, E., Engi, M., Berger, A., Allaz, J., Schwarz, J.O., and Spandler, C., 2008, Prograde metamorphic sequence of REE minerals in pelitic rocks of the Central Alps: implications for allanite–monazite–xenotime phase relations from 250 to 610 C: Journal of Metamorphic Geology, v. 26, no. 5, p. 509–526, https://doi.org/10.1111/j.1525-1314.2008.00774.x.

Jiang, T., Gao, J., Klemd, R., Qian, Q., Zhang, X., Xiong, X., Wang, X., Tan, Z., and Chen, B., 2014, Paleozoic ophiolitic mélanges from the South Tianshan Orogen, NW China: geological, geochemical and geochronological implications for the geodynamic setting: Tectonophysics, v. 612, p. 106–127, https://doi.org/10.1016/j.tecto.2013.11.038.

Jolivet, M., Dominguez, S., Charreau, J., Chen, Y., Li, Y., and Wang, Q., 2010, Mesozoic and Cenozoic tectonic history of the Central Chinese Tian Shan: Reactivated tectonic structures and active deformation: Tectonics, v. 29, no. 6, https://doi.org/10.1029/2010TC002712.

Jourdan, F., Sharp, W.D., and Renne, P.R., 2012, $^{40}Ar/^{39}Ar$ ages for deep (~3.3 km) samples from the Hawaii Scientific Drilling Project, Mauna Kea volcano, Hawaii: Geochemistry Geophysics Geosystems, v. 13, no. 5, https://doi.org/10.1029/2011GC004017.

Kemp, A.I.S., Hawkesworth, C.J., Collins, W.J., Gray, C.M., and Blevin, P.L., 2009, Isotopic evidence for rapid continental growth in an extensional accretionary orogen: The Tasmanides, eastern Australia: Earth and Planetary Science Letters, v. 284, no. 3–4, p. 455–466, https://doi.org/10.1016/j.epsl.2009.05.011.

Khain, E., Bibikova, E., Kröner, A., Zhuravlev, D., Sklyarov, E., Fedotova, A., and Kravchenko-Berezhnoy, I., 2002, The most ancient ophiolite of the Central Asian fold belt: U-Pb and Pb-Pb zircon ages for the Dunzhugur Complex, Eastern Sayan, Siberia, and geodynamic implications: Earth and Planetary Science Letters, v. 199, no. 3, p. 311–325, https://doi.org/10.1016/S0012-821X(02)00587-3.

Klemd, R., John, T., Scherer, E.E., Rondenay, S., and Gao, J., 2011, Changes in dip of subducted slabs at depth: Petrological and geochronological evidence from HP–UHP rocks (Tianshan, NW-China): Earth and Planetary Science Letters, v. 310, no. 1–2, p. 9–20, https://doi.org/10.1016/j.epsl.2011.07.022.

Koppers, A.A., 2002, ArArCALC—software for $^{40}Ar/^{39}Ar$ age calculations: Computers & Geosciences, v. 28, no. 5, p. 605–619, https://doi.org/10.1016/S0098-3004(01)00095-4.

Kruhl, J.H., 1996, Prism- and basal-plane parallel subgrain boundaries in quartz: a microstructural geothermobarometer: Journal of Metamorphic Geology, v. 14, no. 5, p. 581–589, https://doi.org/10.1046/j.1525-1314.1996.00413.x.

Laurent-Charvet, S., Charvet, J., Shu, L., Ma, R., and Lu, H., 2002, Palaeozoic late collisional strike-slip deformations in Tianshan and Altay, Eastern Xinjiang, NW China: Terra Nova, v. 14, no. 4, p. 249–256, https://doi.org/10.1046/j.1365-3121.2002.00417.x.

Laurent-Charvet, S., Charvet, J., Monié, P., and Shu, L., 2003, Late Paleozoic strike-slip shear zones in eastern Central Asia (NW China): new structural and geochronological data: Tectonics, v. 22, no. 2, https://doi.org/10.1029/2001TC901047.

Lee, J.Y., Marti, K., Severinghaus, J.P., Kawamura, K., Yoo, H.S., Lee, J.B., and Kim, J.S., 2006, A redetermination of the isotopic abundances of atmospheric Ar: Geochimica et Cosmochimica Acta, v. 70, no. 17, p. 4507–4512, https://doi.org/10.1016/j.gca.2006.06.1563.

Levashova, N.M., Degtyarev, K., and Bazhenov, M., 2012, Oroclinal bending of the Middle and Late Paleozoic volcanic belts in Kazakhstan: Paleomagnetic evidence and geological implications: Geotectonics, v. 46, no. 4, p. 285–302, https://doi.org/10.1134/S0016852112030041.

Li, P., Sun, M., Rosenbaum, G., Cai, K., and Yu, Y., 2015, Structural evolution of the Irtysh Shear Zone (northwestern China) and implications for the amalgamation of arc systems in the Central Asian Orogenic Belt: Journal of Structural Geology, v. 80, p. 142–156, https://doi.org/10.1016/j.jsg.2015.08.008.

Li, P., Sun, M., Rosenbaum, G., Jourdan, F., Li, S., and Cai, K., 2017, Late Paleozoic closure of the Ob-Zaisan Ocean along the Irtysh shear zone (NW China): Implications for arc amalgamation and oroclinal bending in the Central Asian orogenic belt: Geological Society of America Bulletin, v. 129, no. 5–6, p. 547–569, https://doi.org/10.1130/B31541.1.

Li, P., Sun, M., Rosenbaum, G., Yuan, C., Safonova, I., Cai, K., Jiang, Y., and Zhang, Y., 2018, Geometry, kinematics and tectonic models of the Kazakhstan Orocline, Central Asian Orogenic Belt: Journal of Asian Earth Sciences, v. 153, p. 42–56, https://doi.org/10.1016/j.jseaes.2017.07.029.

Li, P., Sun, M., Shu, C., Yuan, C., Jiang, Y., Zhang, L., and Cai, K., 2019, Evolution of the Central Asian Orogenic Belt along the Siberian margin from Neoproterozoic–Early Paleozoic accretion to Devonian trench retreat and a comparison with Phanerozoic eastern Australia: Earth-Science Reviews, v. 198, p. 102951, https://doi.org/10.1016/j.earscirev.2019.102951.

Li, Q., and Zhang, L., 2004, The P-T path and geological significance of low-pressure granulite-facies metamorphism in Muzhaerte, southwest Tianshan: Acta Petrologica Sinica, v. 20, no. 3, p. 583–594 (in Chinese with the English abstract).

Li, Q.L., Li, X.H., Liu, Y., Tang, G.Q., Yang, J.H., and Zhu, W.G., 2010, Precise U-Pb and Pb-Pb dating of Phanerozoic baddeleyite by SIMS with oxygen flooding technique: Journal of Analytical Atomic Spectrometry, v. 25, no. 7, p. 1107–1113, https://doi.org/10.1039/b923444f.

Li, Q.L., Lin, W., Su, W., Li, X.H., Shi, Y.H., Liu, Y., and Tang, G.Q., 2011, SIMS U-Pb rutile age of low-temperature eclogites from southwestern Chinese Tianshan, NW China: Lithos, v. 122, no. 1, p. 76–86, https://doi.org/10.1016/j.lithos.2010.11.007.

Li, X.H., Liu, Y., Li, Q.L., Guo, C.H., and Chamberlain, K.R., 2009, Precise determination of Phanerozoic zircon Pb/Pb age by multicollector SIMS without external standardization: Geochemistry Geophysics Geosystems, v. 10, no. 4, https://doi.org/10.1029/2009GC002400.

Li, X.H., Tang, G.Q., Gong, B., Yang, Y.H., Hou, K.J., Hu, Z.C., Li, Q.L., Liu, Y., and Li, W.X., 2013, Qinghu zircon: A working reference for microbeam analysis of U-Pb age and Hf and O isotopes: Chinese Science Bulletin, v. 58, no. 36, p. 4647–4654, https://doi.org/10.1007/s11434-013-5932-x.

Lin, W., Faure, M., Shi, Y., Wang, Q., and Li, Z., 2009, Palaeozoic tectonics of the south-western Chinese Tianshan: new insights from a structural study of the high-pressure/low-temperature metamorphic belt: International Journal of Earth Sciences, v. 98, no. 6, p. 1259–1274, https://doi.org/10.1007/s00531-008-0371-7.

Lin, W., Chu, Y., Ji, W., Zhang, Z., Shi, Y., Wang, Z., Li, Z., and Wang, Q., 2013, Geochronological and geochemical constraints for a middle Paleozoic continental arc on the northern margin of the Tarim block: Implications for the Paleozoic tectonic evolution of the South Chinese Tianshan: Lithosphere, v. 5, p. 355–381, https://doi.org/10.1130/L231.1.

Liu, H., Jiang, K., Che, Z., Han, T., and Yuan, Z., 1988, The discovery of Upper Silurian strata and its biologic characteristics in Kekenaike area of Tokxun county, central Tianshan: Geoscience Xinjiang, v. 6, p. 27–40 (in Chinese with the English abstract).

Liu, Y., Hu, Z., Gao, S., Günther, D., Xu, J., Gao, C., and Chen, H., 2008, In situ analysis of major and trace elements of anhydrous minerals by LA-ICP-MS without applying an internal standard: Chemical Geology, v. 257, no. 1, p. 34–43, https://doi.org/10.1016/j.chemgeo.2008.08.004.

Liu, Y., Gao, S., Hu, Z., Gao, C., Zong, K., and Wang, D., 2010, Continental and oceanic crust recycling-induced melt–peridotite interactions in the Trans-North China Orogen: U-Pb dating, Hf isotopes and trace elements in zircons from mantle xenoliths: Journal of Petrology, v. 51, no. 1–2, p. 537–571, https://doi.org/10.1093/petrology/egp082.

Ludwig, K.R., 2003, Isoplot/Ex Version 3.0: A geochronological toolkit for Microsoft Excel: Berkeley, California, Berkeley Geochronological Centre Special Publication, 70 p.

Ma, X., Shu, L., Santosh, M., and Li, J., 2012, Detrital zircon U-Pb geochronology and Hf isotope data from Central Tianshan suggesting a link with the Tarim Block: Implications on Proterozoic supercontinent history: Precambrian Research, v. 206–207, p. 1–16, https://doi.org/10.1016/j.precamres.2012.02.015.

Ma, X., Shu, L., Meert, J.G., and Li, J., 2014, The Paleozoic evolution of Central Tianshan: Geochemical and geochronological evidence: Gondwana Research, v. 25, no. 2, p. 797–819, https://doi.org/10.1016/j.gr.2013.05.015.

Renne, P.R., Mundil, R., Balco, G., Min, K., and Ludwig, K.R., 2010, Joint determination of ^{40}K decay constants and $^{40}Ar^*/^{40}K$ for the Fish Canyon sanidine standard, and improved accuracy for $^{40}Ar/^{39}Ar$ geochronology: Geochimica et Cosmochimica Acta, v. 74, no. 18, p. 5349–5367, https://doi.org/10.1016/j.gca.2010.06.017.

Renne, P. R., Balco, G., Ludwig, K. R., Mundil, R., and Min, K., 2011, Response to the comment by W.H. Schwarz et al. on "Joint determination of ^{40}K decay constants and $^{40}Ar^*/^{40}K$ for the Fish Canyon sanidine standard, and improved accuracy for $^{40}Ar/^{39}Ar$ geochronology" by P.R. Renne et al. (2010): Geochimica et Cosmochimica Acta, v. 75, no. 17, p. 5097–5100, https://doi.org/10.1016/j.gca.2011.06.021.

Renne, P.R., Deino, A.L., Hilgen, F.J., Kuiper, K.F., Mark, D.F., Mitchell, W.S., Morgan, L.E., Mundil, R., and Smit, J., 2013, Time scales of critical events around the Cretaceous-Paleogene boundary: Science, v. 339, no. 6120, p. 684–687, https://doi.org/10.1126/science.1230492.

Rojas-Agramonte, Y., Kröner, A., Alexeiev, D.V., Jeffreys, T., Khudoley, A.K., Wong, J., Geng, H., Shu, L., Semiletkin, S.A., Mikolaichuk, A.V., Kiselev, V.V., Yang, J., and Seltmann, R., 2014, Detrital and igneous zircon ages for supracrustal rocks of the Kyrgyz Tianshan and palaeogeographic implications: Gondwana Research, v. 26, no. 3–4, p. 957–974, https://doi.org/10.1016/j.gr.2013.09.005.

Rong, J.Y., Boucot, A.J., Su, Y.Z., and Strusz, D.L., 1995, Biogeographical analysis of Late Silurian brachiopod faunas, chiefly from Asia and Australia: Lethaia, v. 28, no. 1, p. 39–60, https://doi.org/10.1111/j.1502-3931.1995.tb01592.x.

Rosenbaum, G., 2018, The Tasmanides: Phanerozoic tectonic evolution of eastern Australia: Annual Review of Earth and Planetary Sciences, v. 46, no. 1, p. 291–325, https://doi.org/10.1146/annurev-earth-082517-010146.

Rosenbaum, G., and Mo, W., 2011, Tectonic and magmatic responses to the subduction of high bathymetric relief: Gondwana Research, v. 19, p. 571–582, https://doi.org/10.1016/j.gr.2010.10.007.

Royden, L.H., 1993, The tectonic expression slab pull at continental convergent boundaries: Tectonics, v. 12, no. 2, p. 303–325, https://doi.org/10.1029/92TC02248.

Safonova, I., Seltmann, R., Kroner, A., Gladkochub, D., Schulmann, K., Xiao, W., Kim, J., Komiya, T., and Sun, M., 2011, A new concept of continental construction in the Central Asian Orogenic Belt: Episodes, v. 34, no. 3, p. 186–196, https://doi.org/10.18814/epiiugs/2011/v34i3/005.

Scharf, A., Handy, M.R., Favaro, S., Schmid, S.M., and Bertrand, A., 2013, Modes of orogen-parallel stretching and extensional exhumation in response to microplate indentation and roll-back subduction (Tauern Window, Eastern Alps): International Journal of Earth Sciences, v. 102, no. 6, p. 1627–1654, https://doi.org/10.1007/s00531-013-0894-4.

Schellart, W.P., Freeman, J., Stegman, D.R., Moresi, L., and May, D., 2007, Evolution and diversity of subduction zones controlled by slab width: Nature, v. 446, no. 7133, p. 308–311, https://doi.org/10.1038/nature05615.

Scibiorski, E., Tohver, E., and Jourdan, F., 2015, Rapid cooling and exhumation in the western part of the Mesoproterozoic Albany-Fraser Orogen, Western Australia: Precambrian Research, v. 265, p. 232–248, https://doi.org/10.1016/j.precamres.2015.02.005.

Seltmann, R., Porter, T.M., and Pirajno, F., 2014, Geodynamics and metallogeny of the central Eurasian porphyry and related epithermal mineral systems: a review: Journal of Asian Earth Sciences, v. 79, p. 810–841, https://doi.org/10.1016/j.jseaes.2013.03.030.

Selverstone, J., 2005, Are the Alps collapsing?: Annual Review of Earth and Planetary Sciences, v. 33, no. 1, p. 113–132, https://doi.org/10.1146/annurev.earth.33.092203.122535.

Şengör, A.M.C., and Natal'in, B.A., 1996, Turkic-type orogeny and its role in the making of the continental crust: Annual Review of Earth and Planetary Sciences, v. 24, no. 1, p. 263–337, https://doi.org/10.1146/annurev.earth.24.1.263.

Şengör, A.M.C., Natal'in, B.A., and Burtman, V.S., 1993, Evolution of the Altaid tectonic collage and Palaeozoic crustal growth in Eurasia: Nature, v. 364, no. 6435, p. 299–307, https://doi.org/10.1038/364299a0.

Şengör, A.M.C., Natal'in, B., Sunal, G., and van der Voo, R., 2018, The tectonics of the Altaids: Crustal growth during the construction of the continental lithosphere of central Asia between ~750 and ~130 Ma ago: Annual Review of Earth and Planetary Sciences, v. 46, no. 1, p. 439–494, https://doi.org/10.1146/annurev-earth-060313-054826.

Shi, Y., Liu, D., Zhang, Q., Jian, P., Zhang, F., and Miao, L., 2007, SHRIMP zircon U-Pb dating of the Gangou granitoids, Central Tianshan Mountains, Northwest China and tectonic significances: Chinese Science Bulletin, v. 52, no. 11, p. 1507–1516, https://doi.org/10.1007/s11434-007-0204-2.

Shu, L., Charvet, J., Guo, L., Lu, H., and Laurent-Charvet, S., 1999, A large-scale Palaeozoic dextral ductile strike-slip zone: the Aqqikkudug-Weiya zone along the northern margin of the central Tianshan Belt, Xinjiang, NW China: Acta Geologica Sinica, v. 73, no. 2, p. 148–162, https://doi.org/10.1111/j.1755-6724.1999.tb00822.x.

Shu, L., Charvet, J., Lu, H., and Laurent-Charvet, S., 2002, Paleozoic accretion-collision events and kinematics of ductile deformation in the eastern part of the Southern-Central Tianshan Belt: Acta Geologica Sinica, v. 76, no. 3, p. 308–323.

Shu, L., Wang, B., Zhu, W., Guo, Z., Charvet, J., and Zhang, Y., 2011, Timing of initiation of extension in the Tianshan, based on structural, geochemical and geochronological analyses of bimodal volcanism and olistostrome in the Bogda Shan (NW China): International Journal of Earth Sciences, v. 100, no. 7, p. 1647–1663, https://doi.org/10.1007/s00531-010-0575-5.

Sláma, J., Košler, J., Condon, D.J., Crowley, J.L., Gerdes, A., Hanchar, J.M., Horstwood, M.S.A., Morris, G.A., Nasdala, L., and Norberg, N., 2008, Plešovice zircon—A new natural reference material for U-Pb and Hf isotopic microanalysis: Chemical Geology, v. 249, no. 1–2, p. 1–35, https://doi.org/10.1016/j.chemgeo.2007.11.005.

Sobel, E.R., and Dumitru, T.A., 1997, Thrusting and exhumation around the margins of the western Tarim basin during the India-Asia collision: Journal of Geophysical Research. Solid Earth, v. 102, no. B3, p. 5043–5063, https://doi.org/10.1029/96JB03267.

Stacey, J.S., and Kramers, J.D., 1975, Approximation of terrestrial lead isotope evolution by a two-stage model: Earth and Planetary Science Letters, v. 26, no. 2, p. 207–221, https://doi.org/10.1016/0012-821X(75)90088-6.

Stipp, M., Stünitz, H., Heilbronner, R., and Schmid, S.M., 2002, The eastern Tonale fault zone: a 'natural laboratory' for crystal plastic deformation of quartz over a temperature range from 250 to 700 C: Journal of Structural Geology, v. 24, no. 12, p. 1861–1884, https://doi.org/10.1016/S0191-8141(02)00035-4.

Tan, Z., Agard, P., Monié, P., Gao, J., John, T., Bayet, L., Jiang, T., Wang, X.-S., Hong, T., Wan, B., and Caron, B., 2019, Architecture and P-T-deformation-time evolution of the Chinese SW-Tianshan HP/UHP complex: Implications for subduction dynamics: Earth-Science reviews, v. 197, https://doi.org/10.1016/j.earscirev.2019.102894.

Tang, G.J., Chung, S.L., Hawkesworth, C.J., Cawood, P.A., Wang, Q., Wyman, D.A., Xu, Y.-G., and Zhao, Z.H., 2017, Short episodes of crust generation during protracted accretionary processes: Evidence from Central Asian Orogenic Belt, NW China: Earth and Planetary Science Letters, v. 464, p. 142–154, https://doi.org/10.1016/j.epsl.2017.02.022.

Tian, Z., Sun, J., Windley, B.F., Zhang, Z., Gong, Z., Lin, X., and Xiao, W., 2016, Cenozoic detachment folding in the southern Tianshan foreland, NW China: shortening distances and rates: Journal of Structural Geology, v. 84, p. 142–161, https://doi.org/10.1016/j.jsg.2016.01.007.

Van der Voo, R., Levashova, N.M., Skrinnik, L.I., Kara, T.V., and Bazhenov, M.L., 2006, Late orogenic, large-scale rotations in the Tien Shan and adjacent mobile belts in Kyrgyzstan and Kazakhstan: Tectonophysics, v. 426, no. 3–4, p. 335–360, https://doi.org/10.1016/j.tecto.2006.08.008.

Wang, B., Faure, M., Cluzel, D., Shu, L., Charvet, J., Meffre, S., and Ma, Q., 2006, Late Paleozoic tectonic evolution of the northern West Chinese Tianshan Belt: Geodinamica Acta, v. 19, no. 3–4, p. 237–247, https://doi.org/10.3166/ga.19.237-247.

Wang, B., Chen, Y., Zhan, S., Shu, L., Faure, M., Cluzel, D., Charvet, J., and Laurent-Charvet, S., 2007a, Primary Carboniferous and Permian paleomagnetic results from the Yili Block (NW China) and their implications on the geodynamic evolution of Chinese Tianshan Belt: Earth and Planetary Science Letters, v. 263, no. 3–4, p. 288–308, https://doi.org/10.1016/j.epsl.2007.08.037.

Wang, B., Shu, L.S., Cluzel, D., Faure, M., and Charvet, J., 2007b, Geochemical constraints on Carboniferous volcanic rocks of the Yili Block (Xinjiang, NW China): implication for the tectonic evolution of Western Tianshan: Journal of Asian Earth Sciences, v. 29, no. 1, p. 148–159, https://doi.org/10.1016/j.jseaes.2006.02.008.

Wang, B., Faure, M., Shu, L., de Jong, K., Charvet, J., Cluzel, D., Jahn, B.-m., Chen, Y., and Ruffet, G., 2010a, Structural and geochronological study of high-pressure metamorphic rocks in the Kekesu section (northwestern China): Implications for the late Paleozoic tectonics of the Southern Tianshan: The Journal of Geology, v. 118, no. 1, p. 59–77, https://doi.org/10.1086/648531.

Wang, B., Shu, L., Faure, M., Jahn, B.-m., Cluzel, D., Charvet, J., Chung, S.-l., and Meffre, S., 2011, Paleozoic tectonics of the southern Chinese Tianshan: Insights from structural, chronological and geochemical studies of the Heiyingshan ophiolitic mélange (NW China): Tectonophysics, v. 497, no. 1–4, p. 85–104, https://doi.org/10.1016/j.tecto.2010.11.004.

Wang, B., Cluzel, D., Jahn, B.-m., Shu, L., Chen, Y., Zhai, Y., Branquet, Y., Barbanson, L., and Sizaret, S., 2014a, Late Paleozoic pre-and syn-kinematic plutons of the Kangguer–Huangshan Shear zone: Inference on the tectonic evolution of the eastern Chinese north Tianshan: American Journal of Science, v. 314, no. 1, p. 43–79, https://doi.org/10.2475/01.2014.02.

Wang, B., Liu, H., Shu, L., Jahn, B., Chung, S., Zhai, Y., and Liu, D., 2014b, Early Neoproterozoic crustal evolution in northern Yili Block: Insights from migmatite, orthogneiss and leucogranite of the Wenquan metamorphic complex in the NW Chinese Tianshan: Precambrian Research, v. 242, p. 58–81, https://doi.org/10.1016/j.precamres.2013.12.006.

Wang, B., Zhai, Y., Kapp, P., De Jong, K., Zhong, L., Liu, H., Ma, Y., Gong, H., and Geng, H., 2018, Accretionary tectonics of back-arc oceanic basins in the South Tianshan: Insights from structural, geochronological, and geochemical studies of the Wuwamen ophiolite mélange: Geological Society of America Bulletin, v. 130, no. 3, p. 284–306, https://doi.org/10.1130/B31397.1.

Wang, C.-Y., Yang, Z.-E., Luo, H., and Mooney, W.D., 2004, Crustal structure of the northern margin of the eastern Tien Shan, China, and its tectonic implications for the 1906 M~7.7 Manas earthquake: Earth and Planetary Science Letters, v. 223, no. 1, p. 187–202, https://doi.org/10.1016/j.epsl.2004.04.015.

Wang, H., 2007, Geological Map of Chinese Tianshan and Adjacent Areas: Xi'an, Xi'an Center of Geological Survey, Chinese Geological Survey, scale 1: 1,000,000.

Wang, M., Zhang, J.J., Guowei, Q.I., Zheng, Y., and Liu, K., 2014c, An Early Silurian ductile deformation event in the Sangshuyuanzi shear zone, the southern margin of the Central Tianshan belt, and its geological significance: Acta Petrologica Sinica, v. 30, no. 10, p. 3051–3061 (in Chinese with the English abstract).

Wang, Q.C., Shu, L.S., Charvet, J., Faure, M., Ma, H.D., Natal'in, B., Gao, J., Kroner, A., Xiao, W.J., Li, J.Y., Windley, B., Chen, Y., Glen, R., Jian, P., Zhang, W., Seltmann, R., Wilde, S., Choulet, F., Wan, B., Quinn, C., Rojas-Agramonte, Y., Shang, Q.H., Zhang, W., Wang, B., and Lin, W., 2010b, Understanding and study perspectives on tectonic evolution and crustal structure of the Paleozoic Chinese Tianshan: Episodes, v. 33, no. 4, p. 242–266, https://doi.org/10.18814/epiiugs/2010/v33i4/003.

Wang, Y., Li, J., and Sun, G., 2008, Postcollisional Eastward Extrusion and Tectonic Exhumation along the Eastern Tianshan Orogen, Central Asia: Constraints from Dextral Strike-Slip Motion and $^{40}Ar/^{39}Ar$ Geochronological Evidence: The Journal of Geology, v. 116, no. 6, p. 599–618, https://doi.org/10.1086/591993.

Wang, Z., Qi, Y., and Bergström, S.M., 2007c, Ordovician conodonts of the Tarim Region, Xinjiang, China: Occurrence and use as paleoenvironment indicators: Journal of Asian Earth Sciences, v. 29, no. 5, p. 832–843.

Wartes, M.A., Carroll, A.R., and Greene, T.J., 2002, Permian sedimentary record of the Turpan-Hami basin and adjacent regions, northwest China: Constraints on postamalgamation tectonic evolution: Geological Society of America Bulletin, v. 114, no. 2, p. 131–152, https://doi.org/10.1130/0016-7606(2002)114<0131:PSROTT>2.0.CO;2.

Whitehouse, M.J., Claesson, S., Sunde, T., and Vestin, J., 1997, Ion microprobe U-Pb zircon geochronology and correlation of Archaean gneisses from the Lewisian Complex of Gruinard Bay, northwestern Scotland: Geochimica et Cosmochimica Acta, v. 61, no. 20, p. 4429–4438, https://doi.org/10.1016/S0016-7037(97)00251-2.

Windley, B.F., Alexeiev, D., Xiao, W., Kroner, A., and Badarch, G., 2007, Tectonic models for accretion of the Central Asian Orogenic Belt: Journal of the Geological Society, v. 164, no. 1, p. 31–47, https://doi.org/10.1144/0016-76492006-022.

Wu, H.R., and Li, Z., 2013, Palaeogeographic and tectonic evolution of South Tianshan Ocean: Re-examination of radiolarian cherts and stratigraphic record of southwestern Tianshan: Journal of Palaeogeography, v. 15, no. 3, p. 293–304 (in Chinese with the English abstract).

Xiao, W., 2013, Paleozoic structural deformation and their chronology of middle segment of Tianshan [doctoral dissertation]: Chinese Academy of Geological Sciences, 111 p., http://www.cnki.com.cn.

Xiao, W., Zhang, L., Qin, K., Sun, S., and Li, J., 2004, Paleozoic accretionary and collisional tectonics of the Eastern Tianshan (China): implications for the continental growth of central Asia: American Journal of Science, v. 304, no. 4, p. 370–395, https://doi.org/10.2475/ajs.304.4.370.

Xiao, W., Windley, B.F., Allen, M.B., and Han, C., 2013, Paleozoic multiple accretionary and collisional tectonics of the Chinese Tianshan orogenic collage: Gondwana Research, v. 23, no. 4, p. 1316–1341, https://doi.org/10.1016/j.gr.2012.01.012.

Xiao, W., Windley, B., Sun, S., Li, J., Huang, B., Han, C., Yuan, C., Sun, M., and Chen, H., 2015, A tale of amalgamation of three collage systems in the Permian–Middle Triassic in central-east Asia: Oroclines, sutures, and terminal accretion: Annual Review of Earth and Planetary Sciences, v. 43, no. 1, p. 477–507, https://doi.org/10.1146/annurev-earth-060614-105254.

Xiao, W., Windley, B.F., Han, C., Liu, W., Wan, B., Zhang, J., Ao, S., Zhang, Z., and Song, D., 2018, Late Paleozoic to early Triassic multiple roll-back and oroclinal bending of the Mongolia collage in Central Asia: Earth-Science Reviews, v. 186, p. 94–128, https://doi.org/10.1016/j.earscirev.2017.09.020.

Xu, Z., Wang, Q., Pêcher, A., Liang, F., Qi, X., Cai, Z., Li, H., Zeng, L., and Cao, H., 2013, Orogen-parallel ductile extension and extrusion of the Greater Himalaya in the late Oligocene and Miocene: Tectonics, v. 32, no. 2, p. 191–215, https://doi.org/10.1002/tect.20021.

Yakubchuk, A., 2004, Architecture and mineral deposit settings of the Altaid orogenic collage: a revised model: Journal of Asian Earth Sciences, v. 23, no. 5, p. 761–779, https://doi.org/10.1016/j.jseaes.2004.01.006.

Yang, T., Li, J., Wen, Z., Feng, X., Wang, Y., Sun, G., and Gao, L., 2004, Ductile shearing zones occurring along the northern and southern boundaries of the Central Tianshan Block: Acta Geologica Sinica, v. 78, p. 310–318 (in Chinese with the English abstract).

Yang, T., Li, J., Wang, Y., and Dang, Y., 2009, Late Early Permian (266 Ma) N–S compressional deformation of the Turfan basin, NW China: the cause of the change in basin pattern: International Journal of Earth Sciences, v. 98, no. 6, p. 1311–1324, https://doi.org/10.1007/s00531-008-0396-y.

Yang, T.N., and Wang, X.P., 2006, Geochronology, petrochemistry and tectonic implications of Early Devonian plutons in Kumux area, Xinjiang: Acta Petrologica et Mineralogica, v. 24, no. 1, p. 23–26 (in Chinese with the English abstract).

Yang, T.N., Wang, Y., Li, J.Y., and Sun, G.H., 2007, Vertical and horizontal strain partitioning of the Central Tianshan (NW China): Evidence from structures and $^{40}Ar/^{39}Ar$ geochronology: Journal of Structural Geology, v. 29, no. 10, p. 1605–1621, https://doi.org/10.1016/j.jsg.2007.08.002.

Yang, X., Zhang, L., Tian, Z., and Bader, T., 2013, Petrology and U-Pb zircon dating of coesite-bearing metapelite from the Kebuerte Valley, western Tianshan, China: Journal of Asian Earth Sciences, v. 70–71, p. 295–307, https://doi.org/10.1016/j.jseaes.2013.03.020.

Yi, Z., Huang, B., Xiao, W., Yang, L., and Qiao, Q., 2015, Paleomagnetic study of Late Paleozoic rocks in the Tacheng Basin of West Junggar (NW China): Implications for the tectonic evolution of the western Altaids: Gondwana Research, v. 27, p. 862–877, https://doi.org/10.1016/j.gr.2013.11.006.

Yin, J., Chen, W., Hodges, K.V., Xiao, W., Cai, K., Yuan, C., Sun, M., Liu, L.-P., and van Soest, M.C., 2018, The thermal evolution of Chinese central Tianshan and its implications: Insights from multi-method chronometry: Tectonophysics, v. 722, p. 536–548, https://doi.org/10.1016/j.tecto.2017.11.037.

Zhang, L., Du, J., Lü, Z., Yang, X., Gou, L., Xia, B., Chen, Z., Wei, C., and Song, S., 2013, A huge oceanic-type UHP metamorphic belt in southwestern Tianshan, China: Peak metamorphic age and P-T path: Chinese Science Bulletin, v. 58, no. 35, p. 4378–4383, https://doi.org/10.1007/s11434-013-6074-x.

Zhang, X., Zhao, G., Sun, M., Eizenhöfer, P.R., Han, Y., Hou, W., Liu, D., Wang, B., Liu, Q., and Xu, B., 2016, Tectonic evolution from subduction to arc-continent collision of the Junggar ocean: Constraints from U-Pb dating and Hf isotopes of detrital zircons from the North Tianshan belt, NW China: Geological Society of America Bulletin, v. 128, no. 3–4, p. 644–660, https://doi.org/10.1130/B31230.1.

Zhang, Y., Yuan, C., Sun, M., Long, X., Huang, Z., Jiang, Y., Li, P., Du, L., 2020. Two late Carboniferous belts of Nb-enriched mafic magmatism in the Eastern Tianshan: Heterogeneous mantle sources and geodynamic implications. Geological Society of America Bulletin, https://doi.org/10.1130/B35366.

Zhou, D., Graham, S.A., Chang, E.Z., Wang, B., and Hacker, B., 2001, Paleozoic tectonic amalgamation of the Chinese Tian Shan: Evidence from a transect along the Dushanzi-Kuqa Highway, *in* Hendrix, M. S., and Davis, G. A., eds., Paleozoic and Mesozoic Tectonic Evolution of Central Asia: From Continental Assembly to Intracontinental Deformation: Geological Society of America Memoir 194, p. 23–46, https://doi.org/10.1130/0-8137-1194-0.23.

Zhou, J., Ji, J.Q., Han, B.F., Ma, F., Gong, J.F., Xu, Q.Q., and Guo, Z.J., 2008, $^{40}Ar/^{39}Ar$ geochronology of mafic dykes in north Xinjiang: Acta Petrologica Sinica, v. 24, no. 5, p. 997–1010 (in Chinese with the English abstract).

Zong, K.Q., Chen, J.Y., Hu, Z.C., Liu, Y.S., Li, M., Fan, H.H., and Meng, Y.N., 2015, In-situ U-Pb dating of uraninite by fs-LA-ICP-MS: Science China. Earth Sciences, v. 58, no. 10, p. 1731–1740, https://doi.org/10.1007/s11430-015-5154-y.

Science Editor: Rob Strachan
Associate Editor: Erdin Bozkurt

Manuscript Received 9 May 2019
Revised Manuscript Received 13 December 2019
Manuscript Accepted 26 February 2020

Printed in the USA